

AD-A099 575

PENNSYLVANIA STATE UNIV UNIVERSITY PARK APPLIED RESE--ETC F/G 20/4
AN EXPERIMENTAL AND AN ANALYTICAL STUDY OF THE FLOW FIELD AND H--ETC(U)
MAR 81 K T GUNNARSSON
N00024-79-C-6043
ARL/PSU/TM-81-96

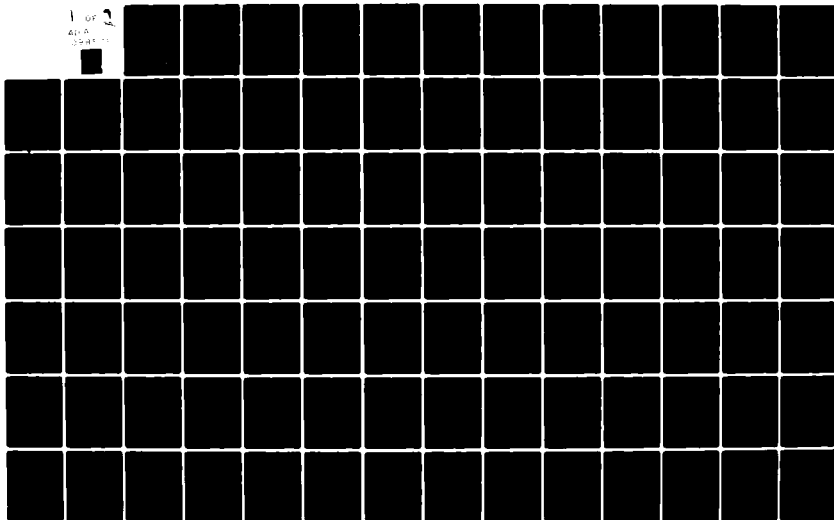
UNCLASSIFIED

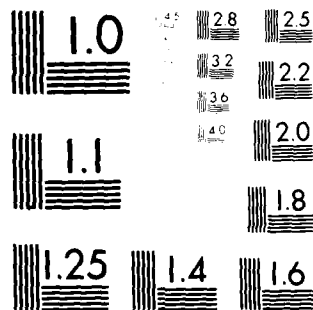
NL

1 of 2

AD-A

034101





MICROCOPY RESOLUTION TEST CHART
NATIONAL BUREAU OF STANDARDS-1963-A

AD A099575

LEVEL

6

AN EXPERIMENTAL AND AN ANALYTICAL STUDY OF THE
FLOW FIELD AND HEAT TRANSFER OF A JET STIRRED BATH

Kristjan T. Gunnarsson

Technical Memorandum
File No. TM 81-96
March 19, 1981
Contract No. N00024-79-C-6043

Copy No. 8

The Pennsylvania State University
Intercollege Research Programs and Facilities
APPLIED RESEARCH LABORATORY
Post Office Box 30
State College, PA 16801

APPROVED FOR PUBLIC RELEASE
DISTRIBUTION UNLIMITED

NAVY DEPARTMENT
NAVAL SEA SYSTEMS COMMAND

DTIC
ELECTE
JUN 2 1981
A

X DTIC FILE COPY

81 6 01 182

UNCLASSIFIED

SECURITY CLASSIFICATION OF THIS PAGE (When Data Entered)

REPORT DOCUMENTATION PAGE		READ INSTRUCTIONS BEFORE COMPLETING FORM
1. REPORT NUMBER ARL/PSU/TM-81-96 ✓	2. GOVT ACCESSION NO.	3. RECIPIENT'S CATALOG NUMBER
4. TITLE (and Subtitle) AN EXPERIMENTAL AND AN ANALYTICAL STUDY OF THE FLOW FIELD AND HEAT TRANSFER OF A JET STIRRED BATH		5. TYPE OF REPORT & PERIOD COVERED MS Thesis, May 1981
7. AUTHOR(s) Kristjan T. Gunnarsson		6. PERFORMING ORG. REPORT NUMBER TM 81-96
9. PERFORMING ORGANIZATION NAME AND ADDRESS The Pennsylvania State University Applied Research Laboratory P. O. Box 30, State College, PA 16801		8. CONTRACT OR GRANT NUMBER(s) N00024-79-C-6043
11. CONTROLLING OFFICE NAME AND ADDRESS Naval Sea Systems Command Department of the Navy Washington, DC 20362		10. PROGRAM ELEMENT, PROJECT, TASK AREA & WORK UNIT NUMBERS
14. MONITORING AGENCY NAME & ADDRESS (if different from Controlling Office)		12. REPORT DATE March 1981
		13. NUMBER OF PAGES 98 pages & figures
		15. SECURITY CLASS. (of this report) Unclassified, Unlimited
		15a. DECLASSIFICATION/DOWNGRADING SCHEDULE
16. DISTRIBUTION STATEMENT (of this Report) Approved for public release, distribution unlimited, per NSSC (Naval Sea Systems Command), 5/11/81		
17. DISTRIBUTION STATEMENT (of the abstract entered in Block 20, if different from Report)		
18. SUPPLEMENTARY NOTES		
19. KEY WORDS (Continue on reverse side if necessary and identify by block number) thesis, flow, field, heat transfer, jet, stirred, bath		
20. ABSTRACT (Continue on reverse side if necessary and identify by block number) The flow field and heat transfer characteristics of a jet-stirred bath are studied using a flow visualization technique and a finite-difference numerical calculation computer code. A description of a water model used in the study is given. The data collection and data reduction phases of the flow visualization method are explained in detail. A description of the TEACH-T computer code for the solution of recirculating turbulent flows (elliptic partial differential equation) is given along with a discussion		

391007

UNCLASSIFIED

SECURITY CLASSIFICATION OF THIS PAGE (When Data Entered)

20. ABSTRACT (continued)

on the present state of mathematical turbulence modeling. Predictions of the variation of the film coefficient along the wall of the bath using both methods are given for jet Reynolds numbers of 43,733 and 30,621.

The flow visualization technique did not give accurate quantitative data. However, its utility in qualitative studies is acknowledged. The TEACH-T computer code gave predictions correct to at least an order of magnitude.

UNCLASSIFIED

SECURITY CLASSIFICATION OF THIS PAGE (When Data Entered)

ABSTRACT

The flow field and heat transfer characteristics of a jet-stirred bath are studied using a flow visualization technique and a finite-difference numerical calculation computer code. A description of a water model used in the study is given. The data collection and data reduction phases of the flow visualization method are explained in detail. A description of the TEACH-T computer code for the solution of recirculating turbulent flows (elliptic partial differential equations) is ~~given~~ along with a discussion on the present state of mathematical turbulence modeling. Predictions of the variation of the film coefficient along the wall of the bath using both methods are given for jet Reynolds numbers of 43,733 and 30,621.

The flow visualization technique did not give accurate quantitative data, However, its utility in qualitative studies is acknowledged. The TEACH-T computer code gave predictions correct to at least an order of magnitude.

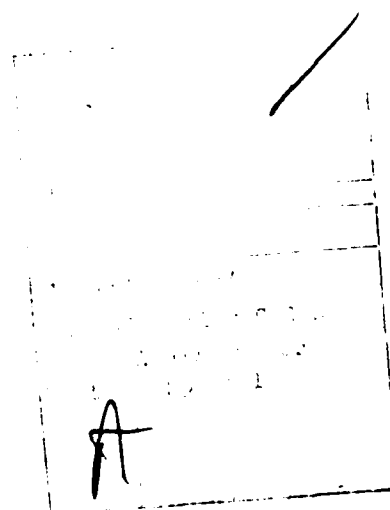


TABLE OF CONTENTS

	<u>Page</u>
ABSTRACT	iii
LIST OF TABLES	vi
LIST OF FIGURES	vii
LIST OF SYMBOLS	ix
ACKNOWLEDGMENTS	xiii
I. INTRODUCTION	1
1.1 Statement of the Problem	1
1.2 Origin and Relevance of the Study	1
1.3 Previous Related Studies	2
1.4 Scope and Purpose of this Study	5
II. FLOW VISUALIZATION TECHNIQUE	6
2.1 Introductory Remarks	6
2.2 Experimental Apparatus	7
2.3 Data Recording	11
2.4 Data Reduction	14
2.5 Explanations and Discussion of the Technique	19
III. NUMERICAL TECHNIQUE	23
3.1 Introduction	23
3.2 A Description of the Numerical Method	24
3.3 Turbulence Model	33
IV. RESULTS AND DISCUSSION	38
4.1 Introductory Remarks	38
4.2 Flow Visualization	38

TABLE OF CONTENTS (CONTINUED)

	<u>Page</u>
4.3 TEACH-T Computer Code	41
4.4 Results	46
V. SUMMARY AND CONCLUSIONS	58
5.1 Summary	58
5.2 Conclusions	59
5.2.1 Flow Visualization	59
5.2.2 Numerical Method	61
REFERENCES	64
APPENDIX A: Experimental Data	66

LIST OF TABLES

<u>Table</u>	<u>Title</u>	<u>Page</u>
I	Conservation Equations Corresponding to the General Conservation Equation	26
II	Data for Experimental and Analytical Investi- gation	39
A.1	Far End Section, $Re_j = 43,733$	68
A.2	Third Downstream Section, $Re_j = 43,733$	70
A.3	Second Downstream Section, $Re_j = 43,733$	73
A.4	First Downstream Section, $Re_j = 43,733$	75
A.5	Far End Section, $Re_j = 30,621$	77
A.6	Third Downstream Section, $Re_j = 30,621$	79
A.7	Second Downstream Section, $Re_j = 30,621$	81
A.8	First Downstream Section, $Re_j = 30,621$	83

LIST OF FIGURES

<u>Figure</u>	<u>Title</u>	<u>Page</u>
1	Schematic of the water loop	8
2	Schematic of model assembly	9
3	Perforated end plate	10
4	A cross section showing the relative positioning of components for particle visualization	12
5	A schematic showing the partitioning of the light plane into sections and the related grid pattern	13
6	A schematic showing the relationship between the apparent (y') and actual distance (y_a) of a particle from the cylinder wall	16
7	Staggered grid pattern	27
8	Control volumes associated with dependent variables. Note that n, e, s and w are shown for the variables calculated at P (w , T , P , k , ϵ)	28
9	Control volume at a solid adiabatic boundary .	32
10	A flow chart of TEACH-T	34
11	Distribution of measuring points in the Far End section ($Re_j = 43,733$)	40
12	Grid Pattern	42
13	Variation of the velocity component parallel to the cylinder wall as measured and calculated in TEACH-T at a distance of 5.5 mm from the wall .	47
14	Velocity field ($Re_j = 43,733$)	50
15	Temperature field ($Re_j = 43,733$)	51

LIST OF FIGURES (CONTINUED)

<u>Figure</u>	<u>Title</u>	<u>Page</u>
16	Film coefficient at the cylinder wall ($Re_j = 43,733$)	52
17	Velocity component parallel to the cylinder wall at a distance of 5.5 mm from the wall ($Re_j = 30,621$)	56
18	Film coefficient along the cylinder wall ($Re_j = 30,621$)	57

LIST OF SYMBOLS

<u>Symbol</u>	<u>Description</u>
$A_P, A_N, A_S, A_W, A_E,$ A'_N, A'_S, A'_W, A'_E	coefficient of the general finite difference equation
A_i	inside area of cylinder wall
B, B'	coefficients of general finite difference equation
C_1, C_2, C_μ	coefficients of turbulence model
C_p	heat capacity of fluid
D	inside diameter of cylinder
D_X	coefficient of finite difference equation
f	Fanning skin friction coefficient
H_f	heat flux through cylinder wall
h, h_w	film heat transfer coefficient at cylinder wall
j_s, j_n	total flux vector components
k_m	fraction of jet momentum dissipated at the wall
k	kinetic turbulence energy
k_{eff}	effective coefficient of heat transport
L	length of cylinder
\dot{m}, \dot{m}_{in}	mass flowrate
n_p, n_w	refractive indexes of plexiglass and water respectively
P	pressure

LIST OF SYMBOLS (CONTINUED)

<u>Symbol</u>	<u>Description</u>
Pe	Peclet number
Pr	Prandtl number
Pr_t	turbulent Prandtl number
r	radial coordinate
R	residual
Re_j	jet Reynolds number
Re_{eq}	equivalent Reynolds number
r_j	jet radius
r_1	inside radius of cylinder
r_2	outside radius of cylinder
St	Stanton number
St_{eq}	equivalent Stanton number
S_ϕ	source term of general conservation equation
T	temperature
T_w	wall temperature
u	axial velocity component or equivalently the velocity component parallel to the cylinder wall
u^+	normalized velocity
U_j	jet velocity
v	radial velocity component
v_s	velocity component perpendicular to solid boundary
v^*	shear velocity

LIST OF SYMBOLS (CONTINUED)

<u>Symbol</u>	<u>Description</u>
V_{jet}	jet velocity
V_{ref}	reference velocity
w	tangential velocity component
x	axial coordinate
y	cartesian coordinate
y_a	actual distance from wall
y'	apparent distance from cylinder wall
y''	radial distance of particle in light plane
y^+	normalized distance from wall
z	cartesian coordinate
ϵ	dissipation rate of turbulence kinetic energy
ρ	fluid density
$\sigma_k, \sigma_\epsilon$	turbulence model coefficients
Γ_ϕ	transport coefficient associated with ϕ
τ_w	wall shear stress
μ_b, μ_w	dynamic viscosity at bulk and wall temperatures respectively
$\mu_{\text{eff}}, \mu_{\text{mol}}, \mu_t$	effective, molecular and turbulent dynamic viscosity respectively
ν	kinematic viscosity
$\theta_1, \theta_2, \theta_3$	angle
ϕ	dependent variable of general conservation equation

LIST OF SYMBOLS (CONTINUED)

<u>Symbol</u>	<u>Description</u>
ϕ_1, ϕ_2, ϕ_3	angles
ϕ	viscous dissipation

ACKNOWLEDGMENTS

The author gratefully acknowledges the support and guidance received from his advisor, Dr. Carl H. Wolgemuth, in the course of this study.

The author is also appreciative of the support obtained from the Applied Research Laboratory of The Pennsylvania State University under contract with the Naval Sea Systems Command.

CHAPTER I

INTRODUCTION

1.1 Statement of the Problem

This study deals with the recirculating flow field in a modified single injector reactor (SIR) with emphasis on the heat transfer characteristics. The SIR consists of a cylinder with perforated plates at both ends. Located centrally on one endplate is a small fluid injector, that when injecting stirs the liquid bath in the cylinder. In this study, the outflow is through the injector endplate. The SIR is studied using two different methods. First, a flow visualization technique is used with the objective of assessing its capabilities and limitations. Second, the TEACH-T computer code is used to solve the Reynolds equations (including the energy equation) governing the flow situation. The experimental and calculated results are compared with each other and available experimental data.

1.2 Origin and Relevance of the Study

The flow field and heat transfer characteristics of a jet stirred bath are of considerable interest, since such a jet mixing process occurs in certain combustion applications. An example of such an application is a boiler reactor. In this case, the fuel is a molten lithium bath and the oxidizer is injected into the reactor. The reaction is exothermic, and the released energy is transferred to a boiler which provides steam to a power cycle.

Previous studies of this system have dealt with overall operation or averaged parameters (heat transfer coefficients). This study is aimed at a more detailed analysis of the flow field and heat transfer in the SIR liquid bath.

1.3 Previous Related Studies

Thomson (1) has developed a correlation for the average heat transfer coefficient for a jet-induced mixing process in a cylindrical chamber. A high momentum heated fluid jet was injected centrally into the liquid bath at one end and low momentum outflow was provided for at that same end. The characteristic system parameters were obtained through an analysis assuming total jet momentum dissipation into shear stress along the cylinder wall and use of the Reynolds analogy. Equivalent Reynolds and Stanton numbers defined in terms of the chamber geometry and jet momentum were introduced, and the resulting correlation was the following:

$$St_{eq} Pr^{.597} = 1.48 ((L/D)^{-.49} (\mu_b/\mu_w)^{-1.185} Re_{eq})^{-.411} . \quad (1)$$

The equivalent Reynolds and Stanton numbers are defined thus:

$$St_{eq} = \frac{h_w}{C_p} \sqrt{\frac{A_i}{\rho \dot{m} U_j}} \quad (2)$$

and

$$Re_{eq} = \frac{L}{\mu_b} \sqrt{\frac{\dot{m} U_j \rho}{A_i}} . \quad (3)$$

Good agreement was obtained between this correlation and the experimental data. This correlation is used for comparison with TEACH-T predictions and experimental results.

Sheu (2) made overall heat transfer and thermodynamic analysis of the SIR and performed experiments using actual alkali metal fuels. He primarily studied different fuel/oxidizer combinations, but he also obtained values for the averaged heat transfer coefficient on the bath side.

Lal (3) made a flow visualization study of the recirculating flow in a SIR using a water model. He did not obtain quantitative data, but made some conclusions regarding the mean and fluctuating nature of the flow field. He also used the TEACH-T computer code to study the effect of different jet Reynolds numbers.

Gosman, et al. (4) present numerical solutions to a number of two dimensional turbulent elliptic (recirculating) flows using the TEACH-T computer code. A comparison between the numerical solutions and experimental data validated the numerical procedure as an acceptable analytical tool. More recently, Whitelaw and Green (5) have published a paper on the isothermal flow in an axisymmetric geometry related to gas turbine combustors. Measurements with laser-Doppler anemometry and calculations using the TEACH-T computer code were obtained. The discrepancies between measured and calculated results were shown to depend more on the distribution of grid nodes than on the turbulence model. In order to get accurate numerical predictions, it was found imperative to use a fine grid pattern for

good resolution in areas of high pressure gradients and high shear. The two-equation k-epsilon turbulence model, which is used in the TEACH-T computer code, has been shown to have inherent drawbacks (6), especially the dissipation equation. Whitelaw and Green found it to be defective in areas of strong recirculation and in near-wall regions. Numerical errors were found to be prevalent in those parts of the flow field where the streamlines were diagonal to the grid pattern. However, the calculations were found to be in reasonable overall agreement with the measurements and the calculation scheme was considered to have practical value.

Rubesin (7), Rubesin and Murphy (8) and Launder (9) give excellent accounts of the present state of turbulence modeling. They show that it is unlikely that a universal turbulence model based on current methods can be developed and point out that, in order to get very accurate predictions, fine tuning of the two-equation k-epsilon model or any other model for that matter is required. Nevertheless, they show that the basic models have their utility in engineering applications.

Numerous authors have reported work done on jet-induced mixing, and both Lal and Thomson provide lists of references in this respect. However, no paper is known that gives a complete analysis of the flow field and heat transfer in jet-stirred baths, let alone under the boundary conditions imposed by the SIR.

1.4 Scope and Purpose of this Study

The main purpose of this study is to obtain data on the variation of the heat transfer coefficient along the wall of the SIR. The actual process in a boiler reactor is extremely complicated; in this study, it is approximated by a water model. The results obtained from the water model study are not conclusive since the heat transfer characteristics of low Prandtl number metals are different from those of water.

In the flow visualization study, the flow is seeded with small polystyrene particles. A high intensity light source with a condensing lens focuses a thin plane of light onto the cylinder axis. A video camera placed above the illuminated plane records the flow field. The videotape can be played back one frame at a time, and knowing the camera speed, the flow velocity can be measured from the displacement of the seeding particles.

The TEACH-T computer code employs a two-equation turbulence model and solves the Reynolds equations using a finite-difference scheme under specified boundary conditions. It gives numerical values for the heat flux at discrete locations along the cylinder wall.

CHAPTER II

FLOW VISUALIZATION TECHNIQUE

2.1 Introductory Remarks

The flow visualization technique used in this study is identical to the one presented by Ekchian and Hoult (10) in all major respects. The same kind of seeding particles were used, but they used high-speed still and movie cameras, whereas a video camera is used here. The purpose of introducing the seeding particles into the flowstream is to visually observe the flow. Because of their finite mass and size (inertia), the seeding particles will only follow the streamlines under certain conditions. The seeding particles used in this study are polystyrene beads. They are almost neutrally buoyant (specific gravity 1.01-1.04) and range in size from 0.5 to 0.8 mm (0.03-0.04 in.) which is rather large. The sinking velocity of the particles is directly proportional to the square of the particle diameter, and to the difference between the particle and fluid density; it is inversely proportional to the fluid viscosity (11). Due to the good match in density and the small residence time of a fluid element in the water model, sinking is almost nonexistent. Allen and Yerman (12) reported that neutral density beads do not alter the flow field; quantitative velocity predictions made from their technique were within five percent of pitot tube data.

From the aforesaid, it is to be expected that the flow visualization technique used will give a reasonable representation of the actual flowfield. However, due to the large size of the seeding particles, they cannot be expected to respond to the higher frequencies of turbulent fluctuations. This is satisfactory because it is not the purpose of this study to utilize this technique for detailed studies of the turbulence quantities. Time-averaged data is all that is required.

2.2 Experimental Apparatus

The experimental apparatus used in this study is the one designed and used by Lal (3). He gives a thorough description of all its components. Figure 1 shows a schematic diagram of the water loop. The major component of the apparatus is the horizontal test chamber (model), which is shown in more detail on Figure 2. The length of the cylinder is 33.6 cm. Its inside diameter is 8.89 cm. and the wall thickness is 0.953 cm. The material is plexiglass. An endplate is shown in Figure 3. The perforations are 0.318 cm. in diameter, set out in a 1.27 cm. by 1.27 cm. matrix. Since the idealized steady state flow pattern is assumed to be axisymmetric, it would have been more appropriate to set them out on a pattern of concentric circles. The porosity ratio is about 5 percent. Outflow is through the nozzle end. The visualization box filled with water removes most of the distortion caused by the curvature of the cylinder when photographically recording. The nozzle is 12.7 cm. long with an outer diameter of 1.27 cm. and a hole diameter of

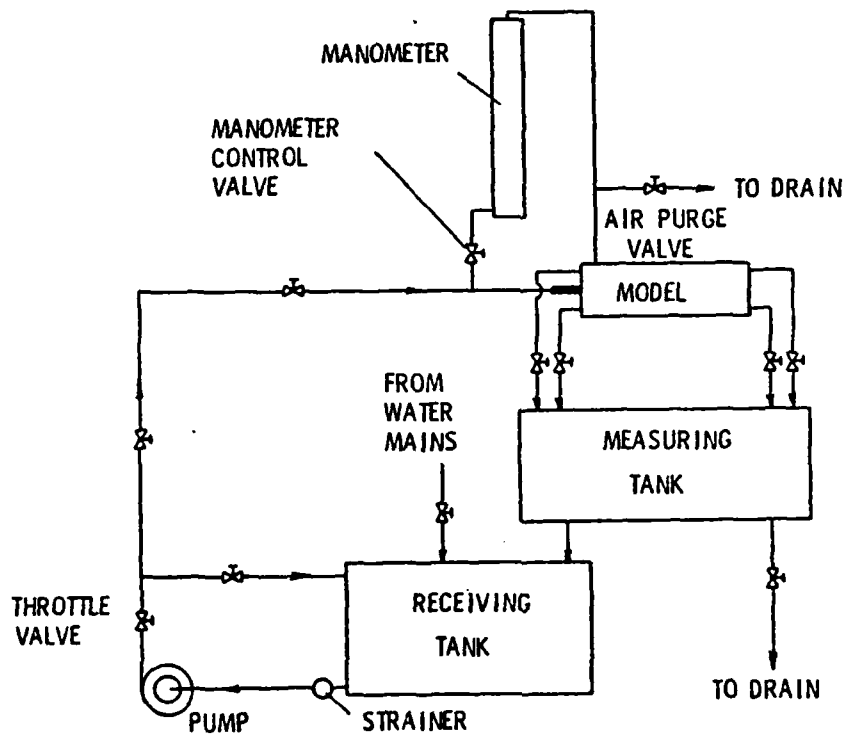


Figure 1 Schematic of the water loop.

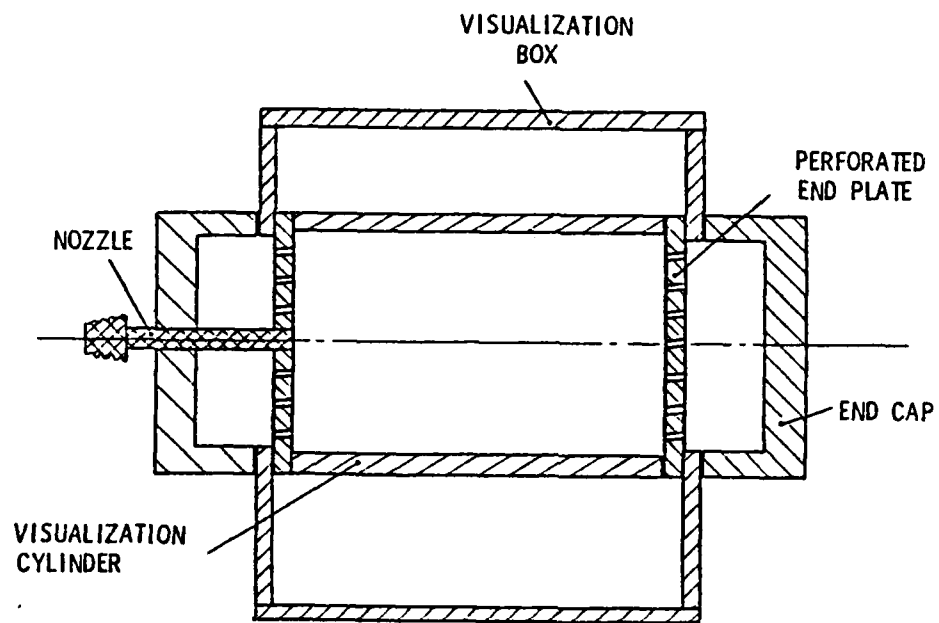


Figure 2 Schematic of model assembly.

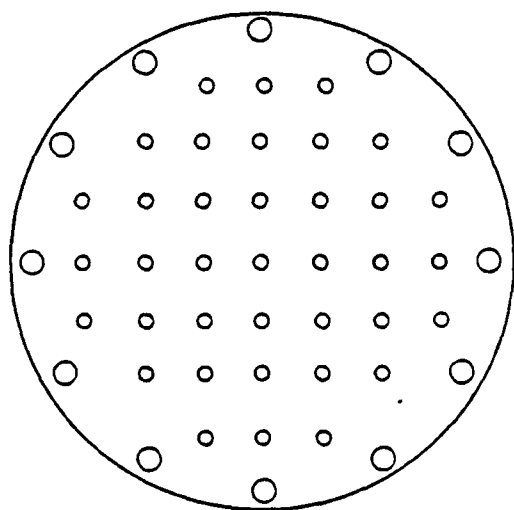


Figure 3 Perforated end plate.

0.253 cm. It was machined from brass bar stock. Other components in the water loop include a measuring tank, a centrifugal pump, valves and a differential manometer.

2.3 Data Recording

A Sony AV-3650 video recording system is used for data collection. This is a standard TV system with a 525 line scan, shoots thirty frames per second, and the recorder can play the tape back one frame at a time. The camera is used at full aperture opening and on full "zoom." A 24-inch Zenith TV set and an 18-inch Hitachi TV set were used for data reduction, the latter one being better since it gives greater picture density.

The flow visualization beads are made clearly visible by exposing them in high intensity light. The scattered light from the particles is recorded by the camera. The light source used is a 1,000 watt General Electric mercury-arc-capillary lamp enclosed by a lamp housing. This housing, mounted on a tripod, contains a system of parallel slits and plano-convex condensing lenses, which enlarge, collimate and define a thin light beam.

Figure 4 shows the relative positioning of components for flow visualization. The camera is approximately five feet above the flow visualization box. Because of the endplate, the time averaged flow pattern is not quite axisymmetric, but a plane containing the axis of the model is assumed to be representative of the flow structure. The light plane is about 0.35 cm. thick. Figure 5 shows how the

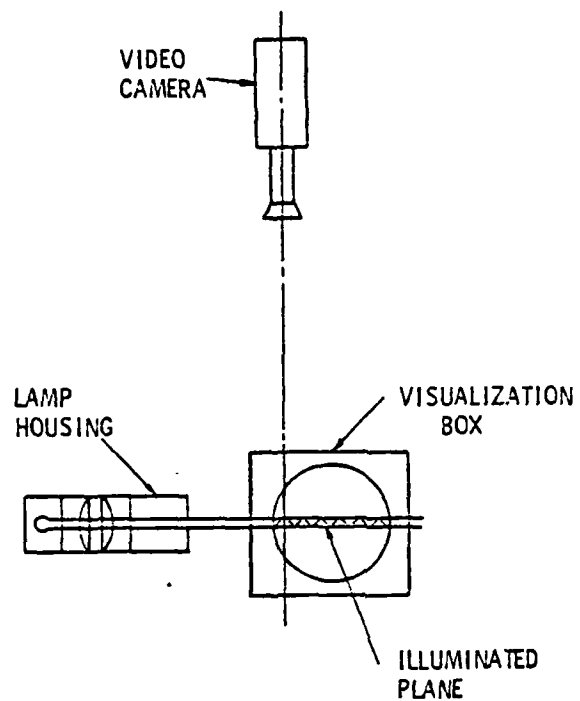


Figure 4 A cross section showing the relative positioning of components for particle visualization.

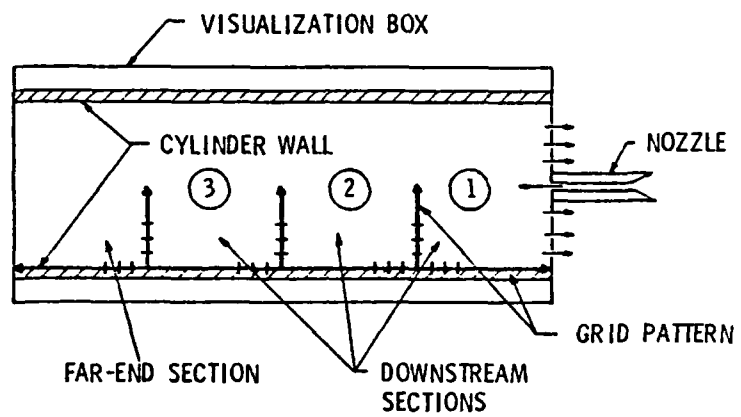


Figure 5 A schematic showing the partitioning of the light plane into sections and the related grid pattern.

cylinder (or the light plane) is divided into four sections. Each section corresponds closely to the field of vision of the camera limited by the condition of sharp focus at full "zoom" and maximum aperture opening and maximum close-up. The grid pattern is drawn on the top plate of the flow visualization box. The light plane is in sharp focus and the grid pattern is not, but markers are drawn so that a scaling factor can be obtained between actual distances and those appearing on the TV screen. A complete recording for one specific flow situation (jet Reynolds number) consists of four segments, each one corresponding to one section. Each segment is five to seven minutes long.

2.4 Data Reduction

The heat transfer characteristics of the SIR through the cylinder wall are of primary concern. The overall flow structure is not of great importance, except for finding dead or stagnation zones and the extensiveness of the recirculating zone. This effort is therefore concentrated at the boundary layer on the cylinder wall. More specifically, the velocity close to the wall is measured. The velocity gradient (or shear stress) and temperature gradient (or film coefficient) are then connected through the Reynolds analogy.

In order to make velocity calculations, the recorded data is played back one frame at a time and viewed on the TV screen. The velocity is found from the observed displacement of a seeding particle, and that requires seeing it in three consecutive frames; the first one to spot it; the second and first one to measure the displacement,

and the third one to verify that it was in the light plane the entire duration of the second frame. The velocity parallel to the wall is then calculated by dividing the component of the measured displacement parallel to the cylinder wall by 1/30 sec. since the camera shoots 30 frames per second.

An exact location of the measured velocity is also needed. Figure 6 shows the path of the scattered light from the seeding particle to the camera. Since the camera is placed high above the lighted plane (about 1.5 m), the light beam entering the camera can be assumed perpendicular to the lighted plane and the top plate of the visualization box. The apparent distance from the wall (y') and the actual (y_a) are related through the following set of equations:

$$\theta_1 = \cos^{-1}\left(\frac{r_1 - y'}{r_2}\right), \quad (4)$$

$$\phi_1 = \pi/2 - \theta_1, \quad (5)$$

$$\phi_2 = \sin^{-1}\left(\frac{n_w}{n_p} \sin \phi_1\right), \quad (6)$$

$$\theta_2 = \sin^{-1}\left(\frac{r_2}{r_1} \sin \phi_2\right), \quad (7)$$

$$\phi_3 = \sin^{-1}\left(\frac{n_p}{n_w} \sin \theta_2\right), \quad (8)$$

$$\theta_3 = \theta_1 + \theta_2 + \phi_2 - \pi, \quad (9)$$

$$y'' = \frac{r_1 \sin \phi_3}{\sin[\pi - (\phi_3 + \theta_3)]} \quad (10)$$

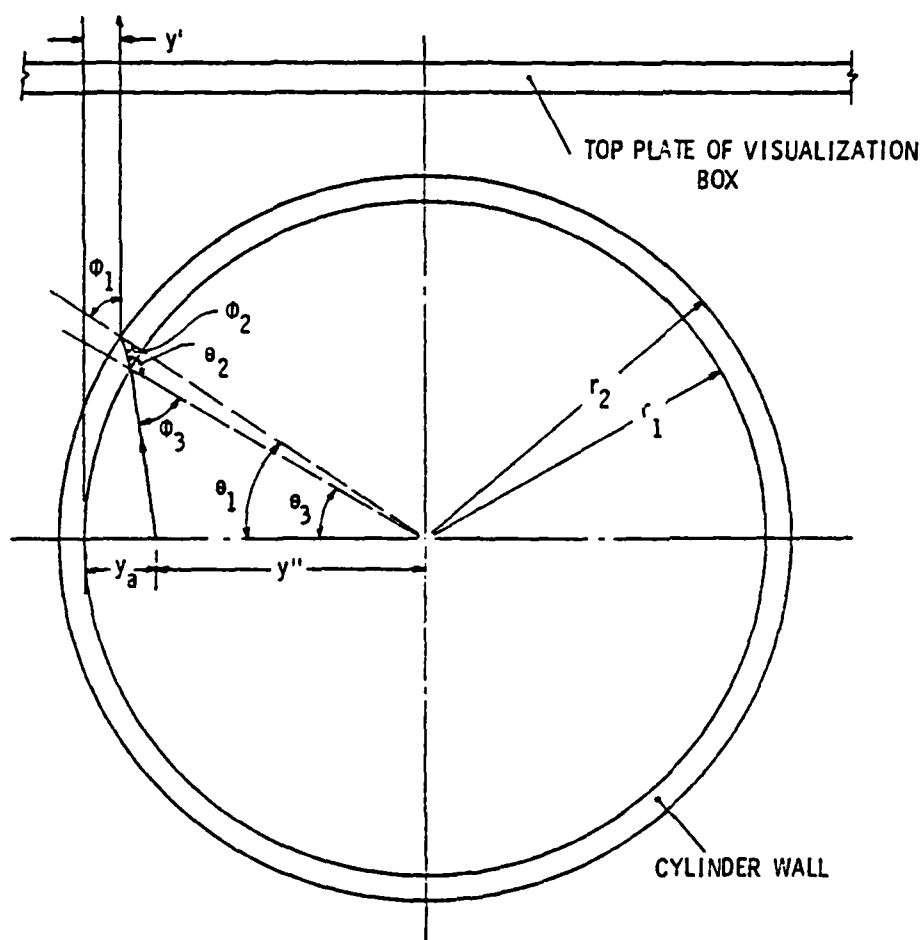


Figure 6 A schematic showing the relationship between the apparent (y') and actual distance (y_a) of a particle from the cylinder wall.

and

$$y_a = r_1 - y'' = r_1 \left\{ 1 - \frac{\sin \phi_3}{\sin[\pi - (\phi_3 + \theta_3)]} \right\} . \quad (11)$$

Many velocity measurements are made in each section. Those measurements that lie close together in space are gathered into one value for a velocity and a distance from the wall. This value is intended to be the time averaged velocity at that point. The velocities are averaged by their absolute values, and the distance is also a simple mean of the individually measured distances. Knowing the velocity parallel to the wall (u) and the distance from it (y_a), the universal law of the wall is used to calculate the local wall shear stress. The universal law of the wall is thus:

$$y^+ \leq 5 \quad u^+ = y^+ , \quad (12)$$

$$5 < y^+ \leq 30 \quad u^+ = 5.0 \ln y^+ - 3.05 \quad (13)$$

and

$$y^+ > 30 \quad u^+ = 2.5 \ln y^+ + 5.5 , \quad (14)$$

where

$$u^+ = \frac{u}{v_*} , \quad y^+ = \frac{y_a v_*}{\nu} \quad \text{and} \quad v_* = \left(\frac{\tau_w}{\rho} \right)^{1/2} .$$

The only unknown in the above equations is the wall shear stress. It can be calculated using a simple fixed point iteration scheme. The local heat transfer coefficient is obtained from the Reynolds analogy:

$$St Pr^{2/3} = f/2, \quad (15)$$

where

$$St = \frac{h}{\rho C_p V_{ref}} \quad \text{and} \quad f = \frac{\tau_w}{1/2 \rho V_{ref}^2}.$$

There is some question as to the appropriate definition of the reference velocity (V_{ref}). In this flow situation, there is neither a free stream nor any clearly defined main bulk flow direction. One possibility is to use the expanded jet velocity, i.e.,

$$V_{ref} = \frac{r_j^2}{r_l^2} V_{jet}. \quad (16)$$

Thomson (1) assumed total jet momentum dissipation into wall shear stress and thus defined a reference velocity. This assumption does not seem quite correct, but he did obtain favorable results with it anyway. This approach is not feasible here, but it is possible to calculate the reference velocity assuming that some fraction of the jet momentum is dissipated at the wall, i.e.,

$$V_{ref} = \frac{r_j}{r_l} V_{jet} k_m^{1/2}, \quad k_m \leq 1. \quad (17)$$

The exact value for k_m is not known, but values can be assumed. It is also possible to estimate it from the difference in the calculated local shear stress and that obtained from the assumption of total jet momentum dissipation into uniform shear stress, i.e.,

$$\tau_w A_i = \dot{m}_{in} V_{jet}. \quad (18)$$

A few words are in order concerning the reliability of the proposed method. The local wall shear stress is calculated using the law of the wall, which is intended for use with flow over plates and pipe and channel flow. In other words, strictly boundary layer flows. It cannot be expected to give accurate predictions for other situations. As a matter of fact, it is in recirculating flows that it breaks down (13). However, boundary layers are always present when a flow is in contact with a solid boundary, and the resulting velocity profile is always assumed to be logarithmic, at least very close to the wall. The Reynolds analogy was also established under similar conditions (plates and channels) and besides, is not accurate. It is therefore apparent that the calculated film coefficients will be rather inaccurate. However, it is hoped that the trend in the variation of the film coefficient over the wall will be predicted.

2.5 Explanations and Discussion of the Technique

The data collection phase of the process employed in this technique is continuous in time. The camera constantly records the observed flow field. However, the data reduction phase, i.e., the conversion of observed particle displacements to a mean velocity, is a sampling process. A detailed description of this process is as follows. The tape is played back one frame at a time. When a particle close to the wall is observed, its location as seen on the first frame is marked on the TV screen. If it is still visible on the second frame, its location is marked again. This displacement of

the particle between frame one and two is used to calculate the velocity. However, before this measurement is accepted, the particle must still be seen on the third frame. This is to verify that the particle was in the light plane the entire duration of the second frame. If it was not, the measurement cannot be considered reliable. This is because, firstly, a particle seen on three frames flows along a path reasonably parallel to the light plane. Secondly, all but the slowest moving particles are not seen on the TV screen as distinct dots but as streaks that are faint toward the ends and bright somewhere in between. The whole streak can be faint if the particle is moving fast or if it is not in the center of the light plane. Seeing the streaks in three consecutive frames is therefore important in establishing valid data.

A certain amount of judgment must be exercised in determining good streaks. A good streak has relatively short tails, is bright in the center, runs almost parallel to the wall and is seen equally bright in three frames. This rarely happens. Sometimes it is difficult to determine whether a small streak or a dot is from one or two particles. This happens if the velocity is low and, consequently, low velocity measurements can be missed. It is preferable to see streaks rather than dots since they are indicative of the path of the particle. When flow reversals occur, the streaks can become very crooked and cannot be accepted. Many bright dots can suddenly be seen if the flow becomes momentarily stagnant, and measurements of zero or very low velocity can be made. This is not done, however,

because upon calculating an average velocity, the ensemble will be biased by a disproportionate amount of low velocity measurements. Also, when a dot appears stationary, it may actually be going either up or down through the light plane. It is also difficult to catch streaks corresponding to a high flow velocity. When that happens, the streaks become very faint and long. Displacement measurements become difficult or very inaccurate at best. High velocity particles are also less likely to remain in the light plane for three frames. A faster camera would be needed.

Due to fluctuations in the flow field, the mean velocity at a certain location must be established from a number of measurements at that point. However, it is unlikely that many particles will flow exactly over the same point, especially if the seeding level is low. When measurements have been completed for a specific section, those that lie close together are assembled into one value for a velocity and a location.

The original plan was to use alumina particles (30-40 microns in diameter) for the flow visualization. They have a high coefficient of reflectivity, but due to their small size, they cannot be recorded by the video camera. The polystyrene beads have to be used therefore, but because they are much larger, they do not allow a high seeding level. In fact, if the seeding level is set too high, they clog the valves in the water loop. The attainable seeding level is also lower at low flow rates or low jet Reynolds numbers than at high flow rates. The seeding level is adjusted by first setting the desired jet Reynolds number (30-40,000), putting a small number of beads into the

receiving tank and then bleeding off the seeded water, replacing it with unseeded water until a steady flowrate is attained without clogging. The resulting seeding level is quite low and an estimate of it is 50-70 particles per liter of water.

The flow situation being studied is very unstable and fluctuating. However, the observed flow field is more stable at high jet Reynolds numbers. In view of what has been said about the technique employed, measurements should be expected to be more reliable when the flow is stable.

In summary, it has been argued that this technique will not give reliable results in regions of stagnation nor high velocity. In general, it is desirable to have a high level of seeding, but because of the large size of the beads, low seeding levels have to be used. This requires more data recording and demands more effort in the data reduction. The flowrate also plays a part, and that can be summarized thus ("+" denoting an advantage and "-" denoting a disadvantage):

- High Re_j : + high level of seeding possible (relatively)
 - + relatively stable flow field
 - long streaks, positioning difficulty
- Low Re_j : - low level of seeding
 - velocity fluctuations
 - + short clear streaks.

CHAPTER III

NUMERICAL TECHNIQUE

3.1 Introduction

TEACH-T is a computer program that solves the conservation equations of fluid mechanics for a given flow situation. It was written and developed at The Imperial College of Science and Technology in the early 1970's. S. V. Patankar and D. B. Spalding published a paper in The International Journal of Heat and Mass Transfer in 1972 describing the essential features of TEACH-T (14). It has been used with some success to predict flows in certain applications (4, 5).

Probably the most important feature of the TEACH-T computer code is that it uses the primitive variables, i.e., the numerical analysis is performed with pressure and velocity as dependent variables and spatial coordinates as independent variables. Earlier methods used the stream function as a dependent variable. The advantage of the primitive variables approach is that it can easily be used in three-dimensional flows, and boundary conditions are easy to formulate.

The Reynolds equations of fluid mechanics (time averaged Navier-Stokes equations) are basically elliptic. Under certain circumstances, important simplifications can be made which render these equations parabolic. In Reference 14, these flow situations

are called parabolic flows. Flow situations requiring the unmodified elliptic equations are called recirculating flows. The flow investigated in this study is of the recirculating type. TEACH-T is really two separate programs, one that solves the parabolic equations (boundary layer type flows) in three dimensions and another one that solves the elliptic equations (recirculating flows) in two or three dimensions. The program itself is not in the form of a subroutine where input data is supplied and the desired output is obtained. For specific flow situations, the program itself is modified. In this case, only the boundaries and their conditions were modified. The numerical formulation and the solution procedure remained the same.

3.2 A Description of the Numerical Method

Descriptions of the TEACH-T computer program and its applications are given in References 4 and 14. TEACH-T solves the conservation equations of fluid mechanics, i.e., mass, momentum, energy, etc. Including mass continuity, the general conservation equation can be written as follows:

$$\frac{\partial}{\partial x} (\rho u \phi) + \frac{1}{r} \frac{\partial}{\partial r} (r \rho v \phi) = \frac{\partial}{\partial x} (\Gamma_{\phi} \frac{\partial \phi}{\partial x}) + \frac{1}{r} \frac{\partial}{\partial r} (r \Gamma_{\phi} \frac{\partial \phi}{\partial r}) + S_{\phi} . \quad (19)$$

This is the elliptic axisymmetric equation, but if $r = 1$ and $\partial r = \partial y$, the equation is converted from cylindrical to cartesian coordinates in two dimensions. ϕ stands for the dependent variable (u, v, T, k, ϵ), ρ is the density and Γ_{ϕ} is a transport coefficient. On the left side of the equal sign are the convection terms. The first two terms on the right side of the equal sign are diffusion terms and the last one

is a source term. The complete set of equations used in TEACH-T is given in Table I. The TEACH-T code does not require that the properties be assumed constant, but in this study, the properties were assumed to be constant. The flow was also assumed to be axisymmetric and, therefore, the tangential momentum equation was omitted and all tangential velocity components were set to zero.

The numerical technique is a finite difference one. The grid pattern used is the so-called "staggered grid" pattern and is shown in Figure 7. A single node is not limited to the intersection of the grid lines, but rather includes the three points P (or N, E, etc.), X and Y enclosed by the boomerang-shaped lines. The u velocity component associated with node P [$u(P)$] is calculated at X, and the v velocity component [$v(P)$] is calculated at Y. All other variables and properties are calculated at P. This arrangement has the convenient feature that velocities are calculated at just the points where they are needed for the calculation of the convective contribution to the balance of ϕ , and the pressure is calculated so as to make it easy to calculate the pressure gradients affecting v and u. The finite difference equations are derived by integrating the conservation equation over the control volume associated with each node. The control volumes are dependent on ϕ as can be seen from Figure 8. The surrounding nodes N, E, S, and W are common to all the control volumes, but the control volumes for u and v each have different n, e, s, and w points.

TABLE I
Conservation Equations Corresponding to the General Conservation Equation

Conservation of:	ϕ	$\Gamma \frac{\phi}{r}$	$S \frac{\phi}{r}$
Mass	1	0	0
Axial Momentum	u	μ_{eff}	$\frac{\partial}{\partial x}(\mu_{\text{eff}} \frac{\partial u}{\partial x}) + \frac{1}{r} \frac{\partial}{\partial r}(\mu_{\text{eff}} r \frac{\partial v}{\partial x}) - \frac{\partial p}{\partial x}$
Radial Momentum	v	μ_{eff}	$\frac{\partial}{\partial x}(\mu_{\text{eff}} \frac{\partial u}{\partial x}) + \frac{1}{r} \frac{\partial}{\partial r}(\mu_{\text{eff}} r \frac{\partial v}{\partial r}) - 2\mu_{\text{eff}} \frac{v}{r^2} - \frac{\partial p}{\partial r} + \rho \frac{w^2}{r}$
Tangential Momentum	w	μ_{eff}	$-(\frac{\mu_{\text{eff}}}{r^2} + \rho \frac{v}{r} + \frac{1}{r} \mu_{\text{eff}} \frac{\partial}{\partial r})w$
Turbulent Kinetic Energy	k	$\mu_{\text{eff}}/\sigma_k$	$\mu_{\text{eff}}\phi - \rho \epsilon$
Turbulence Dissipation Rate	ϵ	$\mu_{\text{eff}}/\sigma_\epsilon$	$\frac{\epsilon}{k}(C_1 \mu_{\text{eff}}\phi - C_2 \rho \epsilon)$

Temperature

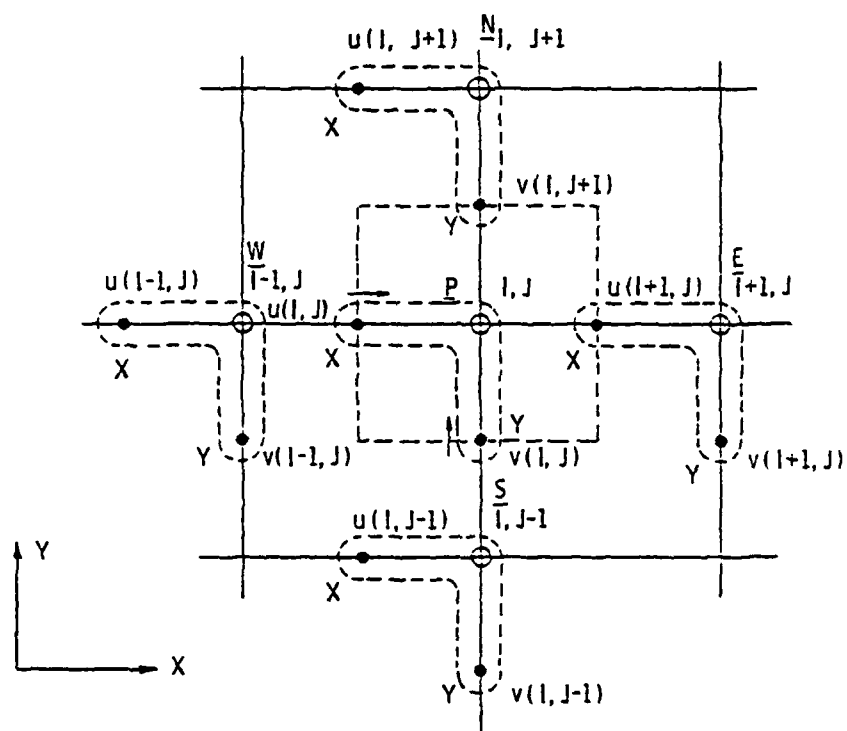
$$T \quad \mu_{\text{eff}}/\text{Pr}_t \quad 0$$

$$\phi = 2\left(\left(\frac{\partial u}{\partial x}\right)^2 + \left(\frac{\partial v}{\partial r}\right)^2 + \left(\frac{v}{r}\right)^2 + \left(\frac{\partial u}{\partial r} + \frac{\partial v}{\partial x}\right)^2 + \left(\frac{\partial w}{\partial x}\right)^2 + \left(r \frac{\partial}{\partial r} \left(\frac{w}{r}\right)\right)^2\right)$$

$$\mu_{\text{eff}} = \mu_{\text{mol}} + \mu_t, \quad \mu_t = C_\mu \rho k^2/\epsilon$$

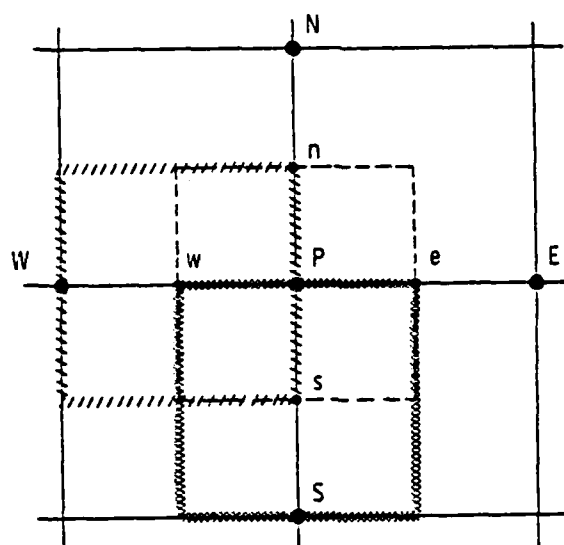
$$C_\mu = 0.09, \quad C_1 = 1.42, \quad C_2 = 1.92$$

$$\text{Pr}_t = 0.9, \quad \sigma_k = 1.0, \quad \sigma_\epsilon = 1.22$$



LOCATION	VARIABLES CALCULATED
O	w, T, P, k, ϵ , FLUID PROPERTIES
X	u
Y	v

Figure 7 Staggered grid pattern.



CONTROL VOLUMES

----- w, T, P, k, ϵ
 ////////////// u
 xxxxxxxxxxxx v

Figure 8 Control volumes associated with dependent variables. Note that n, e, s and w are shown for the variables calculated at P (w, T, P, k, ϵ).

The procedure followed in deriving the finite difference equations starts by the linearization of the convection and diffusion terms of Equation 19. The convection term takes the form,

$$\frac{\partial}{\partial x} (\rho u \phi) = (\rho u) \frac{\partial \phi}{\partial x}, \quad (20)$$

where (ρu) is available from a previous iteration or an initial specification. Similarly, the diffusion term takes the form,

$$\frac{\partial}{\partial x} \left(\Gamma_{\phi} \frac{\partial \phi}{\partial x} \right) = \Gamma_{\phi} \frac{\partial^2 \phi}{\partial x^2}. \quad (21)$$

The convection term is then integrated over the control volume and the resulting equation is,

$$\iiint (\rho u) \frac{\partial \phi}{\partial x} dx dy dz = \Delta y \Delta z [(\rho u)_e \phi_e - (\rho u)_w \phi_w], \quad (22)$$

where: $\phi_e = 1/2 (\phi_E + \phi_P)$ and $\phi_w = 1/2 (\phi_P + \phi_W)$.

Referring to Figures 7 and 8, note that if ϕ is calculated at "P," then:

$$(\rho u)_w = 1/2 [\rho(P) + \rho(W)] u(P), \quad (23)$$

and if ϕ is calculated at "X," then:

$$(\rho u)_w = 1/2 (u(P) + u(W)) \rho(W), \quad (24)$$

and so forth.

The diffusion term is also integrated resulting in the following equation:

$$\iiint \Gamma_{\phi} \frac{\partial^2 \phi}{\partial x^2} dx dy dz = \Delta y \Delta z \left[\Gamma_{\phi,e} \frac{\partial \phi}{\partial x} \Big|_e - \Gamma_{\phi,w} \frac{\partial \phi}{\partial x} \Big|_w \right]. \quad (25)$$

where $\frac{\partial \phi}{\partial x} \Big|_e = \frac{\phi_E - \phi_P}{\Delta x_{E-P}}$ and $\frac{\partial \phi}{\partial x} \Big|_w = \frac{\phi_P - \phi_W}{\Delta x_{P-W}}$.

This eventually leads to an equation of the form (general finite difference equation),

$$A_P \phi_P = A_N \phi_N + A_E \phi_E + A_S \phi_S + A_W \phi_W + B \quad (26)$$

or

$$\phi_P = A'_N \phi_N + A'_E \phi_E + A'_S \phi_S + A'_W \phi_W + B'. \quad (27)$$

As seen from the above equations, the derivatives are approximated using the central difference method. Under conditions of strongly one-directional mass flux, this method leads to erroneous results. This can be seen by taking the corresponding convection and diffusion terms together over to one side of the equal sign of Equation (19) and equating their sum to zero, giving:

$$\rho u \frac{\partial \phi}{\partial x} - \Gamma_\phi \frac{\partial^2 \phi}{\partial x^2} = 0. \quad (28)$$

Employing the central difference method directly to this equation gives:

$$(\rho u)_w \frac{\phi_P - \phi_W}{\Delta x} - \Gamma_\phi|_w \frac{\phi_P - 2\phi_W + \phi_W}{(\Delta x/2)^2} = 0. \quad (29)$$

Solving this equation for ϕ_W , the following is obtained:

$$\phi_W = 1/2 (1 - 1/4 \text{Pe}|_w) \phi_P + 1/2 (1 + 1/2 \text{Pe}|_w) \phi_W, \quad (30)$$

where $\text{Pe}|_w = \frac{\rho u}{\Gamma_\phi} |_w$.

Pe_w is a Peclet number in the sense that it is a ratio of convection to diffusion. When Pe_w goes to zero, ϕ_W tends to $1/2 (\phi_P + \phi_W)$, as it should. When Pe_w approaches positive or negative infinity, ϕ_W

also tends to infinity. This is unfortunate because if Pe_w approaches plus infinity, ϕ_w should approach ϕ_W . To correct this situation, TEACH-T incorporates a so-called high-lateral flux modification procedure. The details of this are somewhat involved, but an explanation is given in References 14 and 15.

The pressure at each node is calculated in TEACH-T by using the mass conservation equation. This procedure is also explained in References 14 and 15, but its main features are as follows. The actual velocity at each node differs from that calculated in each iteration loop by an approximate relationship, which is

$$u_{\text{actual}} = u_{\text{approx.}} + D_x (P_p - P_w), \quad (31)$$

where D_x is a "constant" similar to the A_i ($i = N, E, S, W$) of the general finite difference equation. When this equation is put into the integrated mass conservation equation, an equation for P_p of the same form as the general finite difference equation is obtained. It is solved exactly like the other equations.

One of the best features of TEACH-T is the ease with which the boundary conditions can be applied. It is not necessary to write special equations at the boundaries. Instead, the coefficients in the general finite difference equations need only to be modified. Figure 9 shows a grid node located next to a solid adiabatic boundary. The j_s and j_n are the sum of convection and diffusion fluxes at the boundaries of the control volume obtained by integrating the energy equation, i.e., ϕ stands for the temperature. This gives

$$j_s = (\rho v)_s \phi_s - \Gamma_{\phi,s} \frac{\partial \phi}{\partial y} \Big|_s. \quad (32)$$

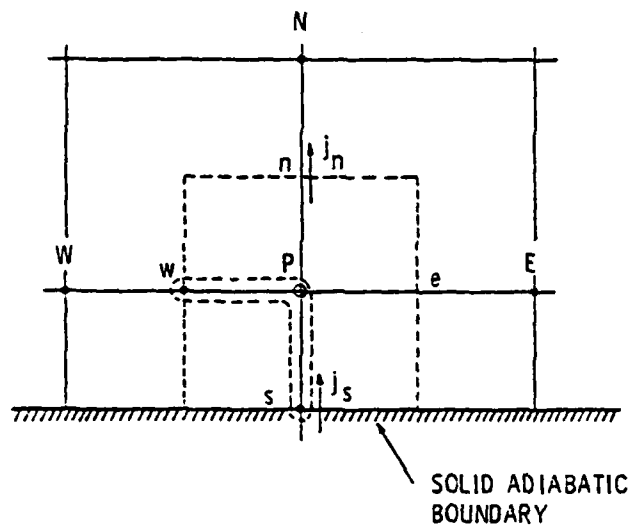


Figure 9 Control volume at a solid adiabatic boundary.

Since the boundary is adiabatic, the gradient of ϕ is zero, and assuming the wall to be impermeable, v_s is also zero. The j_s therefore equals zero, and the coefficient A_s of the energy equation is simply zero.

The solution procedure for the finite difference equations is a so-called line-by-line Gauss-Seidel iteration (14). The values of A_i ($i = N, E, S, W$) in the general finite difference equation are not constant and must be updated as the iteration process develops. The equations are partially solved (partial convergence) for the ϕ s, the A_i are updated, and the cycle is repeated until the termination criteria are satisfied (small residues). Figure 10 shows a flow chart of the computer program.

3.3 Turbulence Model

The most important aspect of numerical calculations of turbulent fluid dynamics is the turbulence model. Over the past forty years or so, a number of turbulence models have been presented in the literature, ranging from simple algebraic ones to highly sophisticated high order models. The present state of turbulence modeling can be seen from the fact that although the higher order models always supersede the simple ones in complexity and computational effort, in certain simple flow situations they are out-performed by the simple ones (7, 8, 9, 13).

All of the turbulence models are based on a mixture of theoretical considerations, ad hoc assumptions and intuition (13). This results in equations with undetermined coefficients. Available experimental data

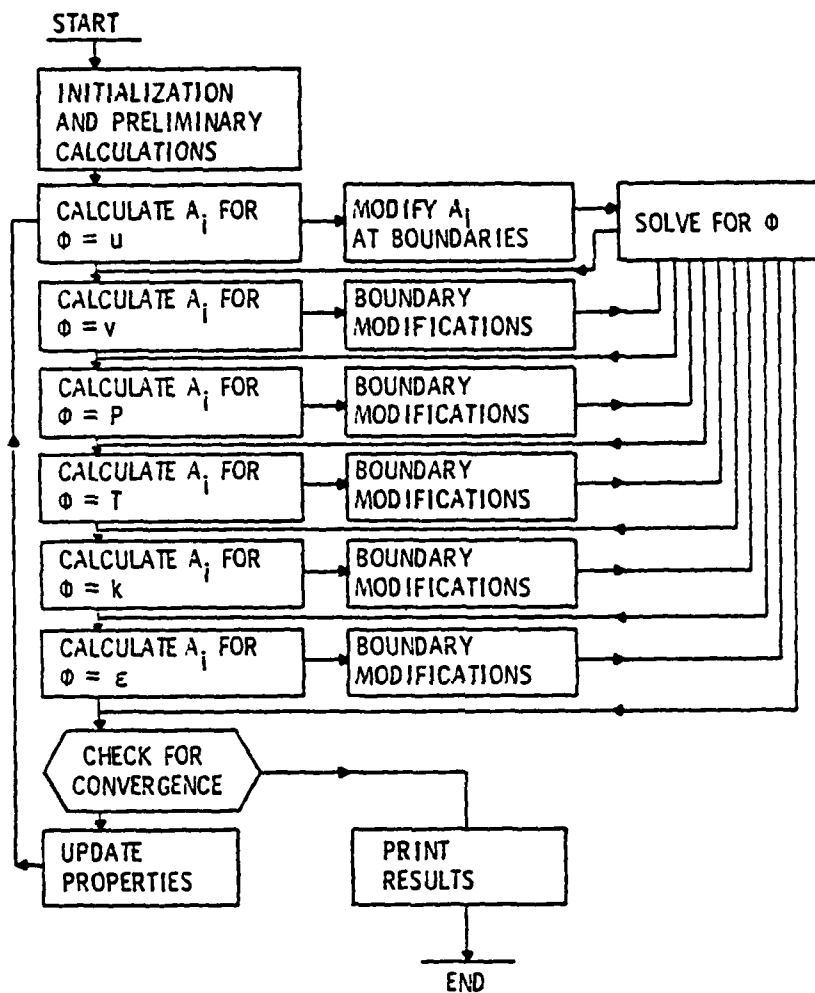


Figure 10 A flow chart of TEACH-T.

is used to determine these coefficients and it is hoped that they will be "universally" applicable. This optimism is questionable, so most researchers hope to develop models fairly reliable over a modest range of conditions, or produce a family of models that engineers can select from, based on the type of flow they are dealing with each time (9). The main effort in this area is currently directed in two areas of study. They are statistical modeling based on the time averaged Reynolds equations (reynolds stresses modeling) and large eddy simulation. Large eddy simulation is more of a research tool, which is too expensive in engineering problem solving, but is hoped to reveal important information about subgrid turbulence structures. Since the turbulence structure at the smallest scales is less dependent on the particular flow situations than the larger scales, it is hoped that "universal" subgrid models will be developed (7).

The simplest of all turbulence models is probably the Prandtl mixing length model. For pipe flows, it works satisfactorily but fails in other applications (13). The next step in complexity is a first order closure model requiring the solution of one partial differential equation where the dependent variable might for instance be the turbulent kinetic energy (8). After some "fine tuning" of coefficients, these models have been able to represent certain fairly simple flow situations well, but are questionable in extension to different situations from those under which the tuning was done (7).

Second order closure models requiring the solution of two partial differential equations have become the standard in the solution of

advanced engineering problems and probably will be the most sophisticated computational design tool generally available in the near future (7, 8). These models are based on the averaged Reynolds equations. In these models, the different scales of turbulence, i.e. those that can be resolved by the finite-difference computational scheme and those that can not be, are ignored by summing the Reynolds stresses into a single stress which then is modelled. Since the time averaging of the Reynolds or Navier-Stokes equations is a drastic simplification, it is doubtful if a universal model will ever be devised on that premise. Nevertheless, these models have a greater potential than the simple ones, but also constitute the upper limit to complexity.

A number of two-equation turbulence models have been developed (7), but the one used in this study is that due to Jones and Launder (13). This model (k-epsilon model) requires the solution of two partial differential equations; one for the turbulence kinetic energy and another one for the dissipation rate of turbulence kinetic energy. Both equations are represented by Equation 19 and the source terms are given in Table I. The main reason for using this model is the fact that it is already incorporated in the TEACH-T code. There is no reason to change that, since that model has been shown to perform just as well as any other (7). One of the reasons that two-equation models are superior to one-equation models (or the algebraic ones) is that they draw upon a wider variety of flow situations for coefficient determination. For instance, the coefficients for dissipation rate are determined in part from experiments dealing with the decay of

isotropic turbulence. Coefficients for pressure fluctuations and instantaneous rate of strain come mainly from experiments in homogeneous turbulence. This reliance on a group of different experiments gives the model a broad base but lessens its capability to represent particular flows in full detail. Various researchers dealing with specific flows have resorted to fine tuning of the coefficients in order to make the model perform better with respect to those flows, and such modifications can be found in the literature (7). The basic model was used in this study and none of the reported modifications were used, since one is never guaranteed better performance in a situation different from that for which the tuning was intended. If a better performance is needed from the turbulence model, the literature must be searched for modifications to the model in flow situations similar to the one being studying. The search may bear no fruit, especially if the flow is of the recirculating type. Most of the turbulence modeling activity comes from the aerospace field where parabolic or boundary layer flows are of main concern. Fine tuning for boundary layer flows may not work for recirculating flows. The only alternative left is then to resort to extensive research using sophisticated equipment (preferably laser-Doppler anemometry) in a study of the flow situation at hand.

CHAPTER IV

RESULTS AND DISCUSSION

4.1 Introductory Remarks

The two methods of analysis described in Chapters II and III i.e., flow visualization and numerical calculation, were employed in an investigation of two flow situations differing only in the jet Reynolds number. The utilization and results of the two methods are discussed and presented in this chapter. The flow situation corresponding to the greater Reynolds number will be described in more detail, since seeding difficulties were encountered in the case of the lesser Reynolds number, thus reducing the accuracy of the data.

4.2 Flow Visualization

The flow field in the SIR was recorded for two different jet Reynolds numbers, namely 43, 733 and 30,621. Table II shows the dimensions of the SIR and operating conditions during data recording. The greater Reynolds number was the highest obtainable with the test apparatus. Maximum seeding without clogging was used. The resulting seeding level is estimated at 50-70 particles per liter of water. This is a very low level of seeding, but acceptable.

Collected data consists of instantaneous velocity measurements and the location of each velocity measurement. Figure 11 shows the location of the measuring points in the far end section (Figure 5) in

TABLE II

Data for Experimental and Analytical Investigation

<u>Variable</u>	
Length of cylinder	340 mm (13.3")
Inner diameter of cylinder	88.9 mm (3.5")
Injector diameter	2.53 mm (0.0995")
Steady state temperature in experiment	32°C (90°F)
Inlet temperature for computer calculations	32°C (90°F)
Cylinder wall temperature for computer calculations	42°C (108°F)
Prandtl no. of water at steady state temperature	5.12
Mass flow rate	.0664, .0465 $\frac{\text{kg}}{\text{s}}$ (527.0, 369.0 $\frac{\text{lbm}}{\text{hr}}$)
Jet momentum	.884, .433 $\frac{\text{kgm}}{\text{s}^2}$ (6.39, 3.13 $\frac{\text{lbm-ft}}{\text{s}^2}$)
Jet Reynolds no.	43,733, 30,621

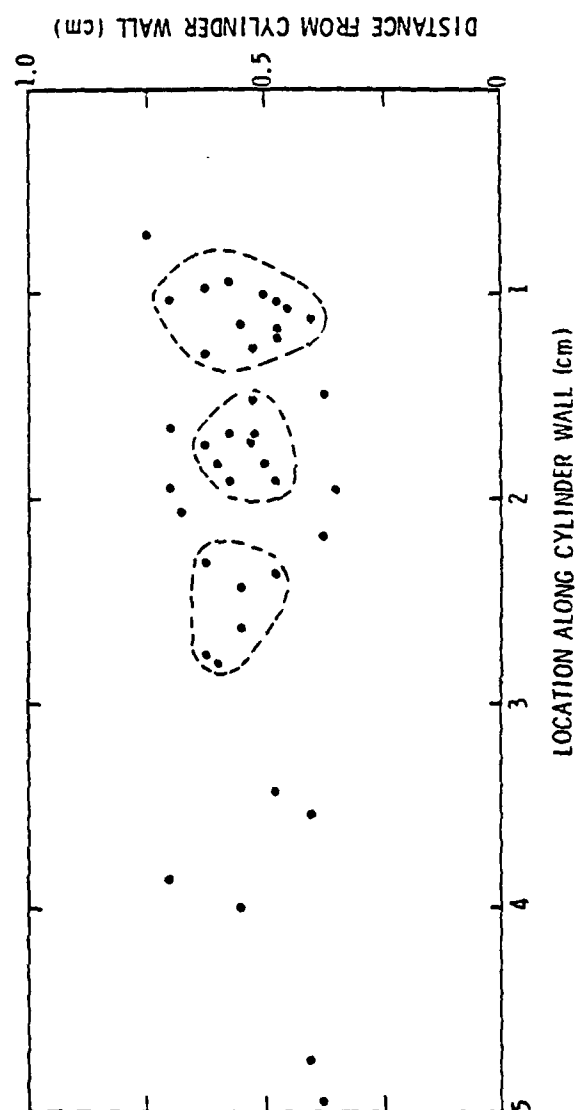


Figure 11 Distribution of measuring points in the Far End section
($Re_j = 43,733$).

the case of the higher Reynolds number. Forty measurements were obtained from seven minutes of data recording. This low number of measurements is due to the low level of seeding that was used. As shown on the figure, those points that are close together are grouped and the coordinates of all the points in each group are averaged. An average velocity corresponding to this location is obtained by averaging the absolute value of the velocity measurements in each group. This averaged velocity is to represent the time-averaged velocity at the averaged location. The averaged velocities that were reduced from the data were based on between six and sixteen velocity measurements. It is not expected that this is sufficient for an accurate estimate. It is just the best that could be done with this technique.

4.3 TEACH-T Computer Code

The TEACH-T computer code was modified to solve the Reynolds equations under the boundary conditions imposed by the SIR. Figure 12 shows the grid pattern that was used, in relation to the boundaries of the SIR. The time-averaged flow structure is assumed to be axisymmetric. However, because of the perforated end plate of the test model, three dimensional effects are present. In order to take some account of this in the numerical calculations without excessive complications, the perforated end plate was modeled as shown in Figure 12. This model was chosen mainly for the sake of its convenience. If the actual perforations in the end plate had been

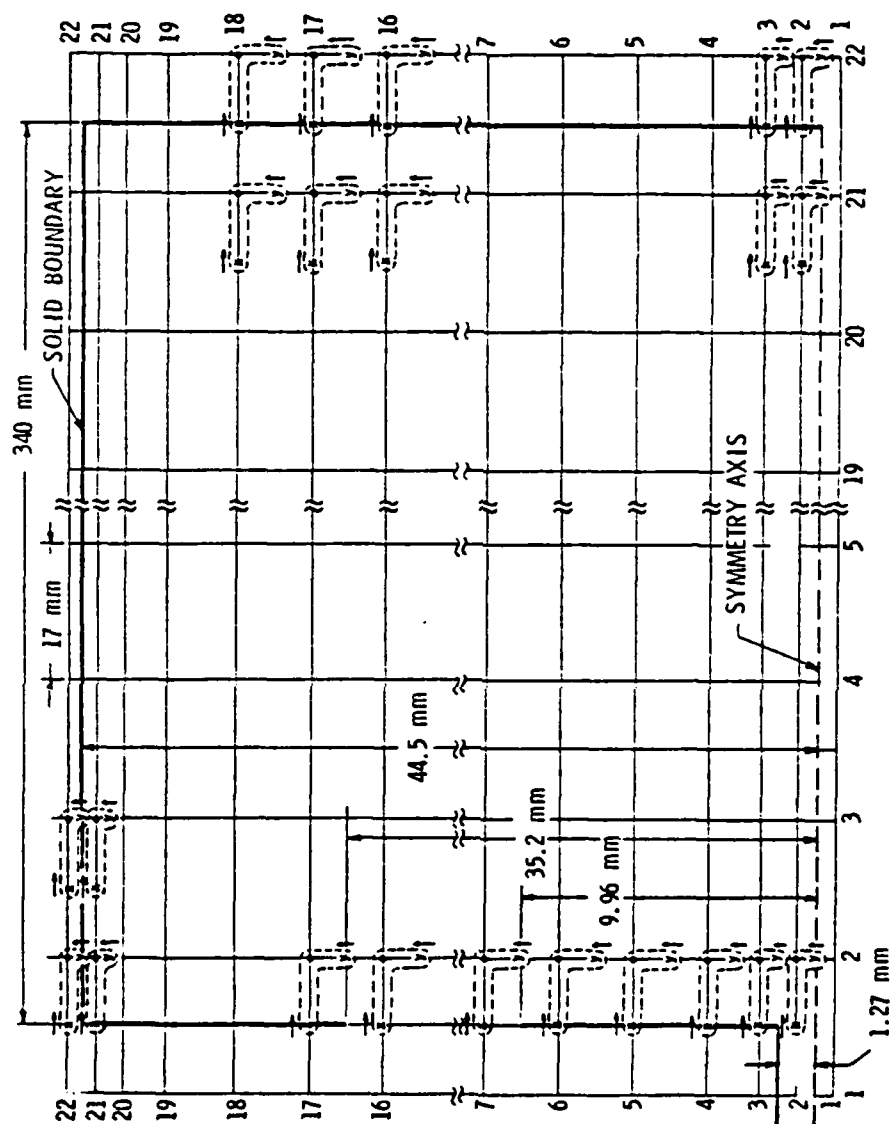


Figure 12 Grid pattern.

used, a greater grid pattern would have been required and it would have been very difficult to specify the amount of liquid flowing out through each hole.

As shown in Figure 12, a 22 x 22 grid pattern was used. This number of grid lines was chosen because it was the maximum number of grid lines possible without extensive modifications of the computer code. In the axial direction, a uniform grid spacing of 17 mm was used. In the radial direction a nonuniform grid spacing was used. Between nodes 4 to 18 the spacing is uniform at 2.52 mm. Between nodes 1 and 2 the spacing is 1.27 mm, and increases uniformly up to node 4. Between nodes 22 and 21 the spacing is 1.1 mm and increases uniformly down to node 18. The opening in the end plate was chosen rather arbitrarily, but also with reference to the visually observed flow pattern at the end plate. Figure 12 also shows the placing of the nodes on the grid lines and the layout of the "boomerangs." The points at which the velocity components are calculated, which are denoted by "X" and "Y" in Figures 7, 8 and 12, are half way between the grid lines.

The use of nonuniform grid spacing is not detrimental to accuracy, nor does it present any computational difficulties. On the contrary, placing the grid nodes in the strategically most important places is considered to be highly instrumental in obtaining a good solution (5,15). No harm is done if this results in a nonuniform grid pattern. Deciding on the strategically best locations is often quite difficult. This usually requires a trial and error procedure. In the present case, the grid lines were placed mainly on the basis of an attempt to obtain

accurate heat transfer rates on the cylinder wall. The small size of the nozzle required a fine grid spacing close to the axis. The radial gap used in the modeling of the end plate was tested for its effect on the heat transfer rates at the cylinder wall. The configuration shown in Figure 12 and another one, where the radial gap was reduced 50 percent from the outer side, were compared and the difference in heat transfer rates was minor.

The flow situation being studied is of the recirculating type. It is governed by a set of elliptic equations (Chapter III). The solution of such equations demands the specification of the boundary conditions everywhere in the solution domain. The hydraulic boundary conditions at a solid impermeable surface require that the velocity component perpendicular to it be set to zero. The same applies at the symmetry axis. Referring to Figure 12, it is seen that the condition of no slip at a solid boundary is not required. A uniform velocity profile was assumed at the nozzle inlet. The boundary conditions at the outlet are by no means certain, but a uniform velocity profile was assumed. This was done in an attempt to simulate the boundary conditions in the SIR. This is indeed arbitrary, but any sort of a developed velocity profile at the outlet is even more so. Forcing the solution to accommodate a uniform velocity profile at the outlet has the effect of a restriction such as a permeable or perforated boundary presents. However, the boundary conditions cannot be determined entirely arbitrarily. They must be somehow physically realistic. Only realistic boundary conditions will yield a convergent solution.

The thermal boundary conditions were prescribed as a constant wall temperature of 42°C and a temperature of the incoming stream of 32°C. Both end walls were assumed adiabatic. The thermal boundary condition at the outflow was assumed fully developed, i.e., no temperature gradient. This is identical to a zero-heatflux boundary and is reasonable since the outgoing internal energy is determined downstream of the boundary.

The boundary conditions for the turbulence kinetic energy (k) and its dissipation rate (ϵ) must be specified. This is difficult since no information concerning the turbulence intensity of the incoming stream is available, but a number of proposals for doing this have been put forth (15). In this study, the turbulence kinetic energy (k) was assumed to be 3 percent of the mean-motion kinetic energy of the jet. The dissipation rate at the nozzle inlet was calculated using the relationship

$$\epsilon = k^{1.5} / (0.005 r_j) , \quad (33)$$

where ϵ denotes the dissipation rate, k is the turbulence kinetic energy of the jet and r_j is the radius of the SIR. At the outlet, k and ϵ were specified in the same manner as at the inlet. It is not warranted to go to great lengths to justify this method of specifying the boundary conditions, since in this case, the calculation domain most likely is insensitive to the boundary conditions. In a complex flow situation such as the present one, there is a substantial generation of both k and ϵ within the domain; therefore, k and ϵ are dominated by the source terms and only weakly affected by the convection terms (15).

The motivation for obtaining the TEACH-T finite difference solution in this study was for reasons of comparison with the data obtained from the flow visualization and other experimental data. However, since the flow situation solved in TEACH-T is only approximately comparable with the actual flow situation and other data, it was not considered proper to impose costly, stringent convergence criteria. Only convergent solutions were accepted, but a maximum of 300 iterations or a maximum normalized residual of 2 percent terminated calculations. The residue is defined as:

$$R = \sum_{\text{nodes}} (\phi_P - A'_N \phi_N - A'_S \phi_S - A'_E \phi_E - A'_W \phi_W - B'). \quad (34)$$

The residue is normalized by either the mass, momentum or energy influx depending on ϕ .

4.4 Results

Figure 13 shows the variation of the velocity parallel to the cylinder wall at a distance of 5.5 mm from it. Both TEACH-T and flow visualization results are shown. The flow visualization data were not all obtained at the same radial location, but the velocity at a particular radial location is obtained by use of the universal law of the wall. The results presented in Figure 13 are for a jet Reynolds number of 43,733.

Apparent from Figure 13 is the fact that the two methods have produced different results. From preceding discussions on the two methods, both can be expected to be in error. However imperfect, TEACH-T has been shown (4, 5) to give reasonable results. On the other hand, the flow visualization technique has more inherent

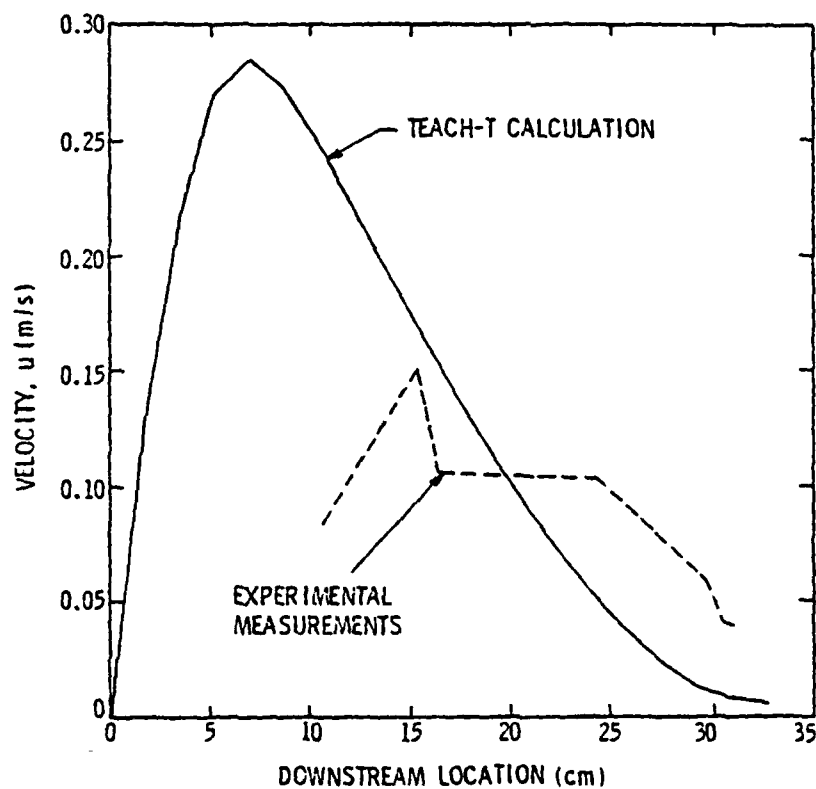


Figure 13 Variation of the velocity component parallel to the cylinder wall as measured and calculated in TEACH-T at a distance of 5.5 mm from the wall.

deficiencies. TEACH-T can therefore be assumed to be closer to the real case, although it must be borne in mind that the two methods do not exactly represent the same flow situation.

The flow visualization technique underpredicts the velocity in the region of high velocity and overpredicts the velocity in the stagnation zone (far end). The flow visualization technique overpredicts the velocity in the stagnation zone mainly for two reasons (Chapter II). First, when the flow velocity is low, the visualization particles become hard to track. Viewing two consecutive frames and observing the particles, it is hard to decide whether the particles have been displaced or new ones have come into the light plane. When in doubt, the latter is assumed and no measurement is made. Secondly, in a region of low velocity it sometimes happens that a large amount of particles indicating no or very little motion at all are observed. Consequently, many measurements of zero or close to zero velocity could be made. There is, however, a tendency to shy away from such situations because the data collection process is a sampling process and a disproportionate amount of zero velocity measurements yields a biased ensemble. Of course there are situations where such measurements are appropriate. Realizing those situations and striking the proper balance of zero velocity measurements is unfortunately difficult.

The reasons for the underprediction of the velocity in the region of high velocity are twofold. First, a particle with a high velocity is less likely than a slow moving one to stay in the light plane for two to three consecutive frames (1/15 to 1/10 sec.). Secondly, fast moving particles leave a faint streak on the TV screen. It can be

difficult to position them and make a displacement measurement. In both cases high velocity measurements are likely to be missed. Velocity measurements close to the nozzle end were not possible due to pronounced three dimensional effects.

Figure 14 shows the velocity field as calculated by TEACH-T. It shows a vortex structure extending more or less all the way from one end to the other. However, the difference in the magnitude of the velocities from the jet to the stagnation zone at the far end is three orders of magnitude (cannot be shown on the figure). The vortex is "strong" only about 40 percent of the length of the cylinder.

Figure 15 shows the temperature field calculated by TEACH-T corresponding to the velocity field of Figure 14.

Figure 16 shows the variation of the film heat transfer coefficient calculated by TEACH-T. Also shown are the heat transfer coefficients based on the Reynolds analogy using the velocities of Figure 13. Since TEACH-T calculates the temperature distribution throughout the domain, the heat flux at the cylinder wall is calculated from,

$$H_f = k_{eff} \frac{T_w - T(I, 21)}{\Delta y}, \quad (35)$$

where k_{eff} is the effective coefficient of heat conduction and Δy is the distance from the wall to the 21st node. The film coefficient is obtained by dividing H_f by a suitable reference temperature difference. In Figure 16, the temperature difference used is $T_{inlet} - T_{wall}$.

The universal law of the wall and the Reynolds analogy can be used to calculate the film coefficient as explained in Chapter II.

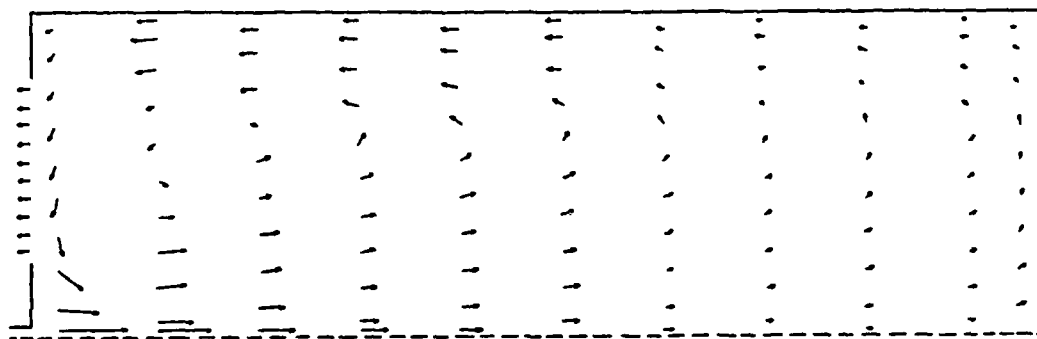


Figure 14 Velocity field ($Re_j = 43,733$).

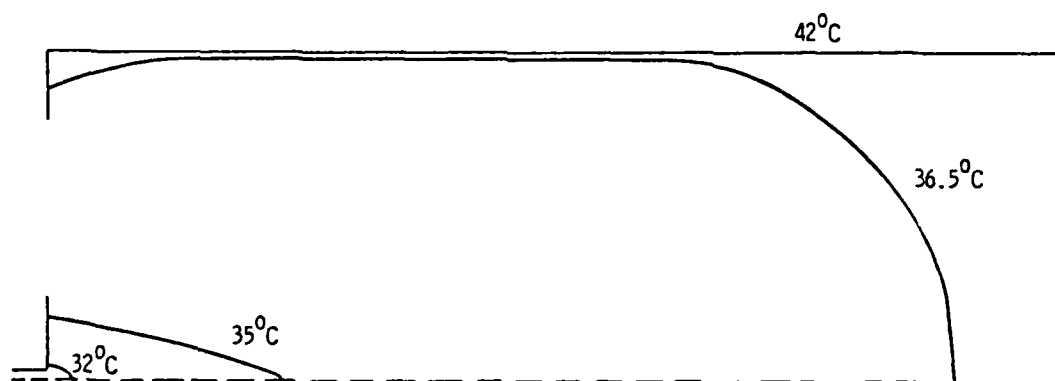


Figure 15 Temperature field ($Re_j = 43,733$).

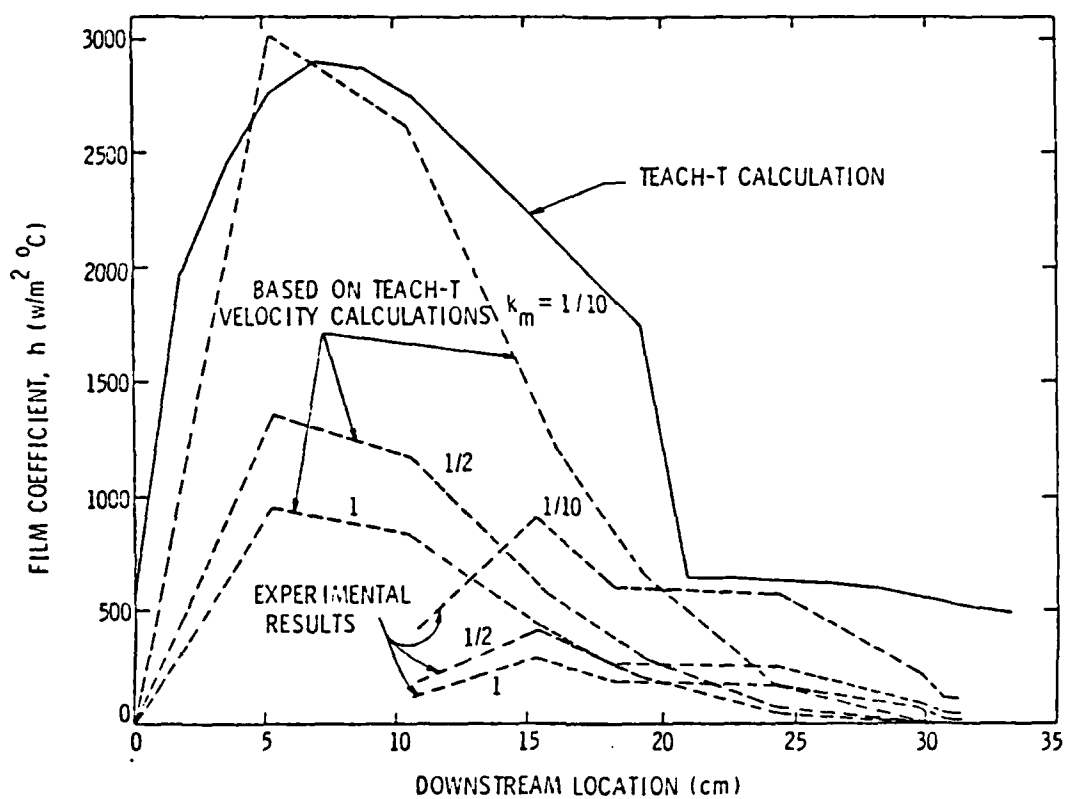


Figure 16 Film coefficient at the cylinder wall ($Re_j = 43,733$).

However, the reference velocity to be used is an undetermined factor. Two different reference velocities were examined and the one based on a fraction of the jet momentum dissipating into shear stress along the cylinder wall was adopted. The reference velocity calculated according to Equation 16 (simple jet expansion) is numerically much lower. The two methods of calculating the reference velocity are in agreement when $k_m = 1/1250$, where k_m denotes the fraction of jet momentum dissipated at the wall. Since the film coefficient is inversely proportional to reference velocity, the method based on Equation 16 gives much higher values for the film coefficient. In view of the results shown in Figure 16, it is not worth the effort to give too much consideration to finding a suitable reference velocity, since the universal law of the wall and the Reynolds analogy apparently are not applicable in this flow situation. Comparing the film coefficients calculated in TEACH-T and those calculated using the TEACH-T velocities in Figure 13, the universal law of the wall, and the Reynolds analogy, considerable discrepancy is obvious. The shape of the curves is similar, but the numerical values are much different, especially in the slowly recirculating stagnation zone. It is also noted that the velocity curves in Figure 13 and the film coefficient curves based on these velocities (Figure 16) have a similar shape.

The heat transfer correlation obtained by Thomson (1) for a jet-induced mixing process was discussed in Chapter I and can be used for comparison with the TEACH-T calculations. The average film coefficient calculated from TEACH-T (Figure 16) is $1,647 \text{ W/m}^2 \text{ } ^\circ\text{C}$. This film coefficient is based on the temperature difference between the incoming

jet stream and the wall temperature, which is 10°C (Table II).

Thomson's correlation is based on the temperature difference between the cylinder wall and the mixing bath temperature. The bath temperature calculated from the TEACH-T solution by volume-weighted averaging of the temperatures over all nodes is 36.2°C . The temperature difference is therefore reduced to 5.8°C , and the corrected film coefficient based on this temperature difference is $2,840 \text{ W/m}^2 \text{ }^{\circ}\text{C}$. An average film coefficient of $3,697 \text{ W/m}^2 \text{ }^{\circ}\text{C}$ is obtained from Thomson's correlation using Equation 1 and the data of Table II (jet Reynolds number of 43,733).

The film coefficient predicted by Thomson's correlation is 1.30 times greater than that predicted by TEACH-T. This discrepancy might in part be due to the fact that the flow situations treated in Thomson's experiment and that solved by TEACH-T are not altogether analogous. Thomson had a cylindrical chamber stirred by a centrally located jet at one end and heat transfer was only through the sidewall. The efflux was through a single small drain pipe located far off center on the injector end. The time-averaged flow field was not axisymmetric. Because of the restricted outflow the flow situation studied by Thomson can be expected to have been more dissipative and therefore enhanced the heat transfer. However, this factor is relatively minor and it can be concluded that TEACH-T gives a prediction at least correct to an order of magnitude.

Sheu (2) measured heat transfer rates in a boiler-reactor using actual alkali metal fuels and halogenated gas oxidizers. Using lithium

fuel and sulfurhexafluoride oxidizer, he measured an average heat transfer coefficient of $1,225 \text{ W/m}^2 \text{ }^\circ\text{C}$ (test H-3 in Reference 2). A serious comparison based on this data cannot be made because two different fluids of greatly different Prandtl numbers are involved. Also, the jet momentum in this study was about four times greater than in Sheu's study. Yet, a note can be made of the order of magnitude.

Figure 17 shows the variation in the velocity parallel to the cylinder wall at a distance of 5.5 mm away from it for the case of a jet Reynolds number of 30,621. The experimental results are not reliable because some intermittent clogging occurred during data collection, even though the seeding level was at an absolute minimum. The extraordinary behavior of the measured velocities has no other plausible explanation than unsuccessful data collection.

Figure 18 shows the variation of the film coefficient for the jet Reynolds number of 30,621. The corrected average film coefficient is $2,179 \text{ W/m}^2 \text{ }^\circ\text{C}$. Thomson's correlation gives $2,985 \text{ W/m}^2 \text{ }^\circ\text{C}$, which is 1.37 times greater.

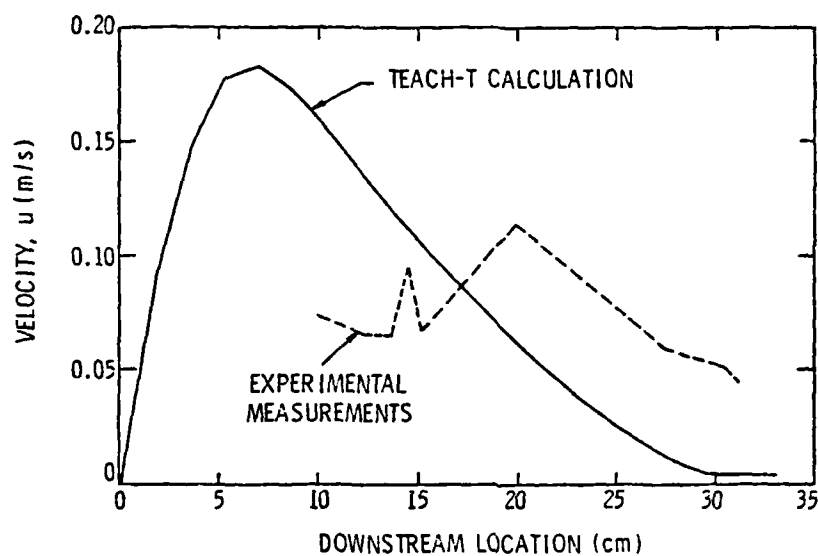


Figure 17 Velocity component parallel to the cylinder wall at a distance of 5.5 mm from the wall ($Re_j = 30,621$).

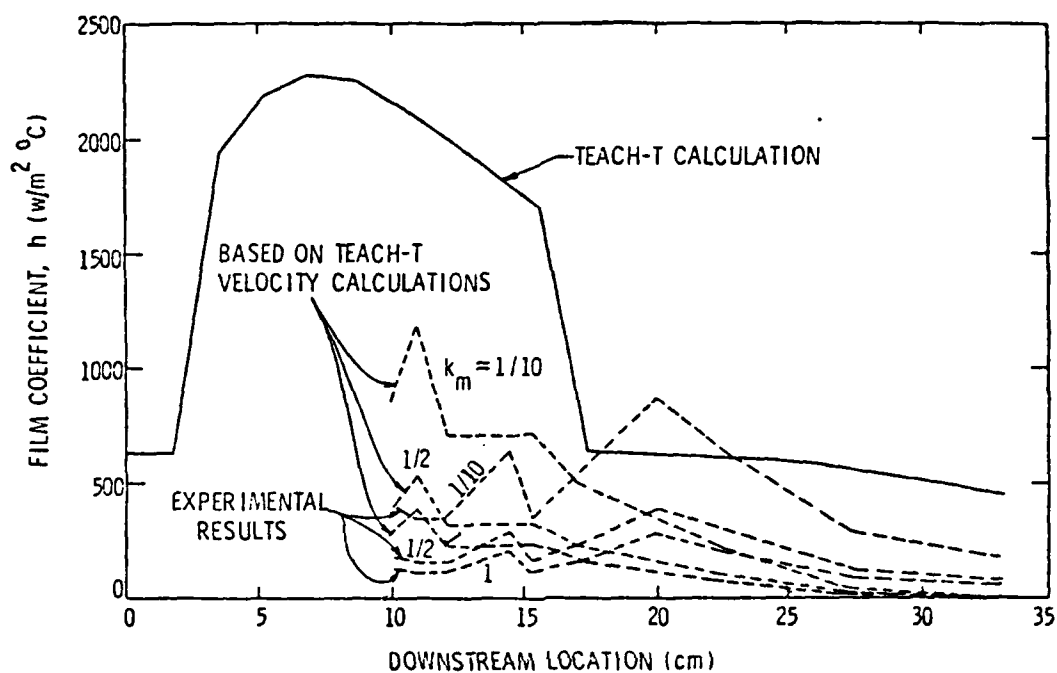


Figure 18 Film coefficient along the cylinder wall ($Re_j = 30,621$).

CHAPTER V

SUMMARY AND CONCLUSIONS

5.1 Summary

The objective of this study was to investigate the recirculating flow field of a single injector reactor (SIR) with an emphasis on heat transfer characteristics. Two different methods of investigation were employed. The purpose of the two methods was to discover their applicability, advantages and disadvantages through trial and to assess their possibilities for use in a more extensive investigation.

The first of the two methods was a flow visualization technique. The fluid was seeded with small polystyrene beads. Their motion was made visible by projecting a thin high intensity light plane through the SIR. The scattered light from the beads was recorded by a video camera thus showing the flow structure in the SIR. A complete description of the entire technique including experimental equipment, data collection and reduction has been given. Two flow fields with different jet Reynolds numbers were studied and the results along with a discussion have been presented.

The second method was a finite-difference numerical solution of the governing equations. The TEACH-T computer code was used and the necessary modifications to account for the geometry and boundary

conditions imposed by the SIR have been described. The computer code was run for the same jet Reynolds numbers used in the experimental study. The solutions obtained were presented and compared with the experimental measurements of this study, as well as the experimental results from the work of others.

5.2 Conclusions

5.2.1 Flow Visualization

The flow visualization technique failed to accurately predict the velocity close to the cylinder wall. This conclusion is based on a comparison with TEACH-T solutions. It has been noted that both methods can be expected to be in some error but in the last chapter it was argued that TEACH-T should be more reliable. A low level of seeding and a slow camera speed are the two basic reasons for this failure.

It has been shown that the data collection process is a selection process. If the seeding level is low, measurements will be few and far between. The greater the seeding level, the more particles will be in the light plane at each instant of time and more measurements will be possible. The measurement density will also be greater (Figure 11). This will result in more accurate time-averaged velocity estimates since the ensemble of measurements on which it is based will be greater and the individual measurements will be closer in spatial location. The danger of ensemble biasing as explained in Chapter II is also attributable to a low seeding level. Given the experimental apparatus used in this study, the seeding level can only be increased

using smaller visualization particles. This in turn requires a stronger light source and photographic equipment with better resolution than the video camera.

The video camera shoots thirty frames per second, but in the last chapter, it was argued that this was too slow for recording the fast moving particles. A slow camera speed requires that the particles remain in the light plane over a relatively long distance. Due to the fluctuating nature of the flow structure a particle does not remain long in the light plane; however, if it does, its trajectory is likely to be very crooked, making velocity measurements difficult. A high-speed movie camera would alleviate this problem.

As can be seen from Figures 16 and 18 in the last chapter, the universal law of the wall and the Reynolds analogy are not valid in this flow situation. A comparison between the film coefficients calculated by TEACH-T and those calculated using TEACH-T velocities, the law of the wall, and the Reynolds analogy shows the latter ones to be off by a considerable amount.

The flow visualization technique used in this study cannot be recommended for detailed analysis demanding accurate quantitative data. Smaller seeding particles, a stronger light source and a high-speed movie camera are needed in such a situation. However, it is reported by Shyam Lal (3) and can be confirmed here that this technique is excellently suited for a qualitative study. By direct visual observation, valuable information about the flow field is immediately available, e.g., jet penetration, jet spreading, the

extent of the recirculation zone, stagnation zones, etc. For a liquid bath stirred by a multitude of jets, which is a much more complicated flow situation than that of the SIR, this method should perform satisfactorily and can be recommended for a qualitative study of such a situation.

5.2.2 Numerical Method

The comparison of TEACH-T solutions and the experimental correlation obtained by Thomson (1), along with results reported in References 4 and 5, show that TEACH-T gives reasonable predictions (at least accurate to an order of magnitude). At present, the state of numerical fluid dynamics is such that not very accurate calculations can be expected, except for well-behaved thoroughly studied flow types (turbulent flows), laminar flows, or inviscid flows (7, 8, 9). Two problems have yet to be resolved; one dealing with the numerical calculations and the more important one dealing with the development of generally applicable and accurate turbulence models.

The high-lateral-flux modification was presented in the last chapter as a correction method when the flow is strongly directional. Whitelaw and Green (5) report difficulties with the high-lateral-flux modification. A mathematically exact solution to this problem is given in Reference 14, but since it is computationally very expensive, it does not represent a satisfactory solution.

The second problem area concerns the grid pattern. Whitelaw and Green (5) have shown that the location of the grid nodes is highly instrumental in obtaining a good solution. Placing the grid nodes

in strategically important places requires either intuition or prior knowledge of the flow situation. Since both may be in limited supply, a fine grid system is required for accurate calculations. The finer the grid pattern, the more expensive the calculations since six equations must be solved at each node corresponding to conservation of mass, axial and radial momentum, energy, turbulence energy and dissipation rate.

A discussion of the present state of turbulence modeling was given in Section 3.3 of Chapter III. Numerical calculations of turbulent flows will only be as accurate as the turbulence model. Better flow predictions can be made when better turbulence models become available.

It is obvious that numerical calculations cannot be expected to give highly accurate solutions. But it has also been shown that the basic models and computation schemes give results correct to at least an order of magnitude and quite possibly better than that. Thus, they can be recommended for use in further studies of jet stirred heat transfer processes. It is expected that numerical calculations can give information about the effects of changing geometric parameters. In the case of a bath stirred by a multitude of jets, the flow structure is three-dimensional and the computer code must be extended to account for that. The necessary equations for such an extension are readily available and are given in Table I (Chapter III); however, the computational effort will be greatly increased. Given a two-dimensional solution for a grid system of a

certain size and assuming that the same number of iterations are required in a three-dimensional study, the required computer time in the three-dimensional study will be "n" times that of the two-dimensional study, where n is the number of nodes in the third dimension.

REFERENCES

1. Thomson, F. X., "Investigation of a Jet-Induced Mixing Heat Transfer Process," M.S. Thesis, The Pennsylvania State University, 1974.
2. Sheu, J. Z., "Alkali Metal-Halogenated Gas Reactions for Underwater Propulsion Systems," M.S. Thesis, The Pennsylvania State University, 1979.
3. Lal, S., "A Water Model Study of Recirculating Flow in a Single Injector Reactor," M.S. Paper, The Pennsylvania State University, 1980.
4. Gosman, A. D., Khalil, E. E. and Whitelaw, J. H., "The Calculation of Two-Dimensional Turbulent Recirculating Flows," First International Symposium on Turbulent Shear Flows, Springer Verlag, Berlin, Heidelberg, 1979, pp. 237-255.
5. Whitelaw, J. H. and Green, A., "Isothermal Flow in Axisymmetric Models of Combustor Geometries," J. of Mech. Eng. Science, Vol. 22, No. 3, 1980.
6. Pope, S. B., Whitelaw, J. H., "The Calculation of Near-Wake Flows," Journal of Fluid Mechanics, Vol. 73, 9 (1976).
7. Rubesin, M. W., "Developments in the Computation of Turbulent Boundary Layers," AGARD Conference Proceedings No. 271 on Turbulent Boundary Layers, AGARD-CP-271, September 1979.
8. Murphy, J. D., Rubesin, M. W., "A Navier-Stokes Fast Solver for Turbulence Modeling Applications," AGARD Conference Proceedings No. 271 on Turbulent Boundary Layers, AGARD-CP-271, September 1979.
9. Launder, B. E., "Reynolds Stress Closure - Status and Prospects," AGARD Conference Proceedings No. 271 on Turbulent Boundary Layers, AGARD-CP-271, September 1979.
10. Ekchian, A. and Hoult, D. P., "Flow Visualization Study of the Intake Process of an Internal Combustion Engine," SAE Technical Paper Series no. 790095, Detroit, February 1979.
11. Merzkirch, W., Flow Visualization, New York, Academic Press, 1974.

12. Allen, M. and Yerman, A. J., "Neutral Density Beads for Flow Visualization," Section 4, Symposium of Flow Visualization, Presentation Summaries, ASME Annual Meeting, Chapter 4, 1960.
13. Launder, B. E. and Spalding, D. B., Mathematical Models of Turbulence, Academic Press, 1972.
14. Patankar, S. V. and Spalding, D. B., "A Calculation Procedure for Heat, Mass and Momentum Transfer in Three-Dimensional Parabolic Flows," Int. J. of Heat and Mass Transfer, Vol. 15, pp. 1787-1806, 1972.
15. Shah, V. L., Sha, W. T., Domanus, H. M., Krazinski, J. L., Miao, C. C., Schmitt, R. C., Vanka, S. P. and Patankar, S. V., "A Numerical Procedure for Calculating Steady/Unsteady, Single-Phase/Two-Phase Three-Dimensional Fluid Flow with Heat Transfer," Nuclear Regulatory Commission Technical Memorandum, NUREG/CR-0782, August 1979.

APPENDIX A
EXPERIMENTAL DATA

Comment on Experimental Data

The light plane was divided into four sections, as explained in Chapter II and shown in Figure 5. Data was collected in all four sections separately. The measurements that were made in each section consisted of grid location (two measurements) and particle displacement. The longitudinal location of a particle was measured positive to the left of the transverse gridline separating the section in which the particle was, and the next section to it, except in the first downstream section where the measurements were positive to the right. The four sections were not equal in width; the far end section was 6 cm wide, the third downstream section was 7.5 cm wide, the second downstream section was 7.45 cm wide and the first downstream section was 12.71 cm wide. The apparent transverse location of a particle was measured from the cylinder wall perpendicular from it. Particle displacement was measured positive when the particle moved from left to right. All measurements given in the following tables are from the TV screen. Reference measurements for conversion from TV screen measurements to real measurements were obtained in each section and are also given.

Table A.1 Far End Section, $Re_j = 43,733$ Longitudinal: $1.0 \text{ cm}_{\text{Real}} \sim 3.5 \text{ cm}_{\text{TV}}$ Transverse: $1.0 \text{ cm}_{\text{Real}} \sim 4.0 \text{ cm}_{\text{TV}}$

Particle Displacement (cm)	Transverse location (cm)	Longitudinal Location (cm)
0.70	2.1	5.3
-0.35	1.4	6.8
1.80	2.3	3.3
0.50	1.9	4.2
0.70	1.9	3.6
-0.40	2.3	6.7
0.33	2.2	4.0
1.0	2.5	3.4
0.5	2.0	6.4
0.5	2.4	6.4
1.2	1.9	8.3
1.2	2.8	3.6
-0.4	1.9	6.7
0.3	2.5	6.1
0.75	1.8	3.7
0.45	1.5	7.6
0.90	3.0	2.5
-0.80	2.8	6.8
0.50	2.5	4.5
0.30	2.5	8.1

Table A.1 Far End Section, $Re_j = 43,733$ (Continued)

Particle Displacement (cm)	Transverse Location (cm)	Longitudinal Location (cm)
0.30	2.3	5.9
0.70	2.0	3.5
0.30	2.8	13.5
0.30	2.5	9.7
0.35	2.2	9.2
0.30	1.5	17.3
0.45	2.2	8.5
0.50	2.8	5.8
0.50	2.7	7.2
0.25	2.4	9.8
0.50	1.6	3.9
0.80	1.5	5.2
0.35	1.9	12.0
-0.45	2.1	5.9
-0.20	1.9	4.1
0.25	1.6	16.6
-0.25	2.1	4.4
0.70	2.1	6.0
-0.40	1.6	12.4
0.30	2.2	14.0

Table A.2 Third Downstream Section, $Re_j = 43,733$ Longitudinal: $1.0 \text{ cm}_{\text{Real}} \sim 3.11 \text{ cm}_{\text{TV}}$ Transverse: $1.0 \text{ cm}_{\text{Real}} \sim 3.78 \text{ cm}_{\text{TV}}$

Particle Displacement (cm)	Transverse Location (cm)	Longitudinal Location (cm)
0.95	1.70	3.30
1.85	3.20	9.50
2.15	3.00	3.10
0.60	2.50	8.70
2.20	3.40	3.70
1.15	2.90	5.50
1.50	2.00	9.90
1.70	2.30	4.50
0.65	2.90	3.70
0.40	2.30	4.80
0.90	2.20	4.40
0.25	3.30	1.80
2.50	2.40	6.30
2.20	2.50	4.10
2.10	2.50	5.80
1.30	2.70	4.20
1.10	1.60	6.60
1.35	2.70	5.50
1.00	3.00	5.40
2.10	2.40	9.80

Table A.2 Third Downstream Section, $Re_j = 43,733$ (Continued)

Particle Displacement (cm)	Transverse Location (cm)	Longitudinal Location (cm)
1.70	3.10	3.40
0.70	2.50	9.40
0.50	2.30	11.10
1.10	2.50	12.4
0.45	2.50	3.70
-0.75	2.30	3.90
1.45	2.75	7.20
0.40	3.00	7.30
1.05	2.50	9.50
1.10	2.70	8.50
0.95	2.10	12.50
1.55	2.20	7.40
1.55	2.00	5.70
0.75	2.30	10.50
0.30	2.30	4.90
0.00	2.20	3.45
1.30	2.60	6.50
0.85	1.60	6.99
1.05	2.70	6.00
0.70	2.00	6.60
0.40	2.40	6.60

Table A.2 Third Downstream Section, $Re_j = 43,733$ (Continued)

Particle Displacement (cm)	Transverse Location (cm)	Logitudinal Location (cm)
1.65	2.50	6.40
0.95	2.30	4.50

Table A.3 Second Downstream Section, $Re_j = 43,733$ Longitudinal: $1.0 \text{ cm}_{\text{Real}} \sim 3.15 \text{ cm}_{\text{TV}}$ Transverse: $1.0 \text{ cm}_{\text{Real}} \sim 3.75 \text{ cm}_{\text{TV}}$

Particle Displacement (cm)	Transverse Location (cm)	Longitudinal Location (cm)
1.80	2.30	4.60
1.60	2.30	9.20
1.30	1.80	7.0
2.35	2.00	6.5
0.65	1.50	6.4
1.50	2.20	5.4
1.90	2.30	8.5
1.80	2.50	7.0
0.85	2.20	8.1
2.30	2.00	6.5
2.30	2.40	4.0
0.75	1.30	5.5
0.50	2.00	8.2
3.35	2.50	5.5
3.00	2.50	6.1
1.80	2.50	5.3
-0.90	3.80	14.5
0.65	3.10	5.3
0.95	2.50	5.8
1.40	3.00	13.3

Table A.3 Second Downstream Section, $Re_j = 43,733$ (Continued)

Particle Displacement (cm)	Transverse Location (cm)	Longitudinal Location (cm)
0.15	2.10	12.0
-1.30	3.30	6.7
2.25	3.50	10.7
1.05	3.10	8.8
1.00	2.40	9.3
0.70	2.50	5.6
0.85	2.80	4.1
1.70	2.70	14.5
1.30	2.00	11.4
0.90	2.10	10.1
1.15	3.00	12.3
1.25	2.20	12.7
1.40	2.90	4.6
0.95	2.90	6.7
1.45	3.30	5.0
1.20	2.50	9.9
1.20	3.20	4.0

Table A.4 First Downstream Section, $Re_j = 43,733$ Longitudinal: $1.0 \text{ cm}_{\text{Real}} \sim 2.70 \text{ cm}_{\text{TV}}$ Transverse: $1.0 \text{ cm}_{\text{Real}} \sim 3.25 \text{ cm}_{\text{TV}}$

Particle Displacement (cm)	Transverse Location (cm)	Longitudinal Location (cm)
0.60	2.3	14.0
-0.45	4.1	5.7
0.65	1.5	8.3
-0.35	3.0	8.2
-0.60	4.1	5.7
-0.45	2.1	8.6
0.60	4.0	4.6
0.90	3.4	3.0
1.05	2.0	5.7
1.30	4.0	7.0
1.50	2.5	3.4
1.45	1.4	6.9
0.60	3.6	9.6
0.70	2.9	4.5
0.90	3.0	10.0
0.50	2.7	11.5
0.45	2.7	5.8
0.35	2.6	5.1
0.75	2.7	2.8

Table A.4 First Downstream Section, $Re_j = 43,733$ (Continued)

<u>Particle</u>	<u>Displacement</u> <u>(cm)</u>	<u>Transverse Location</u> <u>(cm)</u>	<u>Longitudinal Location</u> <u>(cm)</u>
	0.55	2.1	7.3
	0.45	1.9	8.5

Table A.5 Far End Section, $Re_j = 30,621$ Longitudinal: $1.0 \text{ cm}_{\text{Real}} \sim 6.73 \text{ cm}_{\text{TV}}$ Transverse: $1.0 \text{ cm}_{\text{Real}} \sim 7.13 \text{ cm}_{\text{TV}}$

<u>Particle Displacement (cm)</u>	<u>Transverse Location (cm)</u>	<u>Longitudinal Location (cm)</u>
-1.2	6.0	19.5
1.2	4.3	- 9.5
-0.9	5.0	13.7
1.9	2.9	9.7
1.9	5.2	- 7.7
1.4	4.6	- 4.6
2.5	6.2	8.3
-1.5	4.0	-10.0
0.9	5.0	17.4
1.0	3.4	- 9.7
1.1	5.5	21.5
1.3	4.0	9.2
2.1	5.8	12.8
0.5	5.2	15.3
1.2	5.1	22.0
-1.8	5.1	7.7
1.7	3.5	- 8.3
0.8	6.3	8.8

Table A.5 Far End Section, $Re_j = 30,621$

<u>Particle Displacement (cm)</u>	<u>Transverse Location (cm)</u>	<u>Longitudinal Location (cm)</u>
1.0	4.0	- 7.0
1.4	2.6	- 7.5
1.4	6.7	- 5.5
0.9	3.3	- 7.0
1.5	7.1	- 9.5
0.55	5.6	12.5
1.2	4.4	16.8
1.05	4.8	12.2
1.0	5.6	17.6
1.4	7.5	- 4.2
1.5	7.5	- 5.7
1.25	4.2	12.2

Table A.6 Third Downstream Section, $Re_j = 30,621$ Longitudinal: $1.0 \text{ cm}_{\text{Real}} \sim 6.77 \text{ cm}_{\text{TV}}$ Transverse: $1.0 \text{ cm}_{\text{Real}} \sim 7.35 \text{ cm}_{\text{TV}}$

Particle Displacement (cm)	Transverse Location (cm)	Longitudinal Location (cm)
1.30	5.4	2.3
1.85	5.9	0.0
3.20	2.2	8.2
-3.00	4.8	- 5.2
-1.90	6.0	13.0
1.10	2.9	21.5
2.30	7.3	- 5.0
2.10	4.2	14.8
2.50	4.3	11.1
2.10	5.4	5.8
2.30	4.5	- 5.3
3.00	5.5	- 8.0
2.10	5.6	- 5.5
2.50	5.2	5.9
2.20	4.3	9.6
2.05	4.5	20.5
2.50	5.4	6.0
4.50	6.3	- 7.0
2.90	4.8	9.0
2.70	8.0	- 6.2

Table A.6 Third Downstream Section, $Re_j = 30,621$ (Continued)

Particle Displacement (cm)	Transverse Location (cm)	Longitudinal Location (cm)
1.80	4.6	8.2
2.30	4.9	10.3
1.10	3.3	6.5
-2.00	8.2	- 8.2
1.50	5.1	10.0
1.80	5.5	- 5.0
2.50	4.0	8.0
2.40	2.1	13.1
1.30	5.3	19.2
2.00	6.2	18.3
1.50	4.8	11.4
2.60	5.0	- 7.3
1.90	5.9	13.0
3.40	7.0	- 0.5
1.60	4.5	4.3
1.70	4.8	- 6.9

Table A.7 Second Downstream Section, $Re_j = 30,621$ Longitudinal: $1.0 \text{ cm}_{\text{Real}} \sim 6.82 \text{ cm}_{\text{TV}}$ Transverse: $1.0 \text{ cm}_{\text{Real}} \sim 7.62 \text{ cm}_{\text{TV}}$

Particle Displacement (cm)	Transverse Location (cm)	Longitudinal Location (cm)
-1.30	5.5	6.4
0.80	5.9	15.0
1.40	5.9	25.5
2.30	3.6	22.0
3.00	6.6	24.0
3.70	5.0	21.2
3.10	7.1	24.0
2.80	7.1	7.9
3.00	8.6	18.0
1.90	7.4	5.6
1.50	6.1	11.5
3.20	4.9	11.6
2.50	6.1	6.4
1.00	6.2	24.1
1.45	6.4	22.3
-1.50	6.5	25.0
-1.40	7.3	12.8
-1.80	7.1	15.3
-0.70	4.8	11.3
-2.40	7.6	8.8

Table A.7 Second Downstream Section, $Re_j = 30,621$ (Continued)

Particle Displacement (cm)	Transverse Location (cm)	Longitudinal Location (cm)
-2.00	6.5	10.0
-1.70	6.4	5.0
1.40	6.5	14.3
3.00	6.4	6.5
2.50	7.5	9.6
2.90	7.4	20.0
1.50	6.6	13.0
2.60	8.0	6.8
1.80	5.0	8.8
1.20	7.4	2.1
2.40	7.2	6.8
-1.80	5.6	12.3
3.30	6.3	20.7
2.00	7.2	- 4.5
3.10	5.1	18.5

AD-A099 575

PENNSYLVANIA STATE UNIV UNIVERSITY PARK APPLIED RESE--ETC F/G 20/4
AN EXPERIMENTAL AND AN ANALYTICAL STUDY OF THE FLOW FIELD AND H--ETC(U)
MAR 81 K T GUNNARSSON
N00024-79-C-6043
ARL/PSU/TM-81-96

UNCLASSIFIED

NL

2 1

4-1-81
UNCLASSIFIED

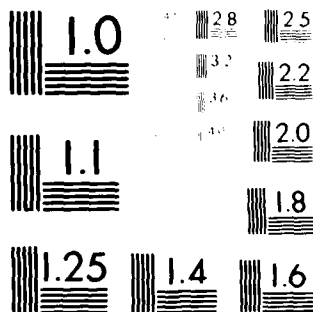


END

DATE

6-81

DTIC



MICROCOPY RESOLUTION TEST CHART
NBS 1010-A

Table A.8 First Downstream Section, $Re_j = 30,621$ longitudinal: $1.0 \text{ cm}_{\text{Real}} \sim 6.72 \text{ cm}_{\text{TV}}$ Transverse: $1.0 \text{ cm}_{\text{Real}} \sim 7.37 \text{ cm}_{\text{TV}}$

<u>Particle Displacement (cm)</u>	<u>Transverse Location (cm)</u>	<u>Longitudinal Location (cm)</u>
-0.60	6.9	- 4.4
-1.10	6.7	7.3
-1.80	5.4	20.7
-1.50	6.4	8.3
-1.30	8.7	7.6
-1.50	5.3	16.0
-1.00	4.2	19.0
-1.30	7.8	19.7
2.40	7.9	23.2
1.10	5.8	15.7
2.50	7.8	9.1
3.20	8.6	- 5.7
1.50	6.0	16.8
1.00	6.5	15.4
2.40	8.5	12.0
1.50	9.1	14.1
1.30	4.9	- 4.4
-0.80	8.8	13.8
2.0	6.8	- 7.5
1.60	6.5	4.7

Table A.8 First Downstream Section, $Re_j = 30,621$ (Continued)

<u>Particle Displacement (cm)</u>	<u>Transverse Location (cm)</u>	<u>Longitudinal Location (cm)</u>
0.90	5.8	5.7
-1.10	7.4	10.7
1.30	8.8	15.6
1.30	6.3	14.6
1.30	3.9	17.5
1.15	5.5	13.6
2.30	8.1	20.2
1.30	7.4	25.9
2.30	6.8	16.9
1.50	6.1	22.5
1.00	7.9	15.6
-1.10	6.6	13.4
2.50	6.3	- 9.2
2.40	7.5	20.9
1.50	8.5	9.0
2.35	6.7	17.4
2.65	6.7	17.3
-1.40	6.4	24.5
-1.40	9.0	28.3
-1.50	8.5	- 7.7
-1.00	5.7	26.9

Table A.8 First Downstream Section, $Re_j = 30,621$

<u>Particle Displacement (cm)</u>	<u>Transverse Location (cm)</u>	<u>Longitudinal Location (cm)</u>
1.60	5.1	20.8
1.10	8.8	23.4
1.50	7.6	22.6
1.40	6.3	16.1

DISTRIBUTION

Commander (NSEA 0342)
Naval Sea Systems Command
Department of the Navy
Washington, DC 20362

Copies 1 and 2

Commander (NSEA 9961)
Naval Sea Systems Command
Department of the Navy
Washington, DC 20362

Copies 3 and 4

Defense Technical Information Center
5010 Duke Street
Cameron Station
Alexandria, VA 22314

Copies 5 through 10

DATE
FILMED
-8